Czech Technical University in Prague
Faculty of Electrical Engineering

Department of Microelectronics
Field of Study: Electronics and Communication

The Study of Antiferromagnetic Layers

DIPLOMA THESIS

Author: Bc. Karolína Veselá
Supervisor: doc. RNDr. Jan Voves, CSc.
Consultant: Ing. Vít Novák, CSc.

ČVUT
ČESKÉ VYSOKÉ UČENÍ TECHNICKÉ V PRAZE

ZADÁNÍ DIPLOMOVÉ PRÁCE

I. OSOBNÍ A STUDIJNÍ ÚDAJE

Příjmení: **Veselá** Jméno: **Karolína** Osobní číslo: **483890**

Fakulta/ústav: **Fakulta elektrotechnická**

Zadávající katedra/ústav: **Katedra mikroelektroniky**

Studijní program: **Elektronika a komunikace**

Specializace: **Elektronika**

II. ÚDAJE K DIPLOMOVÉ PRÁCI

Název diplomové práce:

Studium antiferomagnetických vrstev

Název diplomové práce anglicky:

The Study of Antiferromagnetic Layers

Pokyny pro vypracování:

1. Prostudujte spintronické struktury založené na antiferomagnetických materiálech a jejich možné aplikace
2. Proveďte shrnutí metod přípravy a transportních vlastností epitaxního materiálu CuMnAs.
3. Proveďte měření transportních a magnetoelektrických vlastností GaMnAs v širokém rozmezí teplot a analyzujte korelace těchto vlastností se změnami magnetického uspořádání a dalších materiálových parametrů.

Seznam doporučené literatury:

[1] P. Wadley et al.: Electrical switching of an antiferromagnet. Science, 351, 587-590 (2015) [2] F. Krizek, et al.: Molecular beam epitaxy of CuMnAs. Phys. Rev. Materials 4, 014409 (2020)

Jméno a pracoviště vedoucí(ho) diplomové práce:

doc. RNDr. Jan Voves, CSc. katedra mikroelektroniky FEL

Jméno a pracoviště druhé(ho) vedoucí(ho) nebo konzultanta(ky) diplomové práce:

Datum zadání diplomové práce: **24.01.2023** Termín odevzdání diplomové práce: **26.05.2023**

Platnost zadání diplomové práce: **22.09.2024**

doc. RNDr. Jan Voves, CSc. podpis vedoucí(ho) práce	prof. Ing. Pavel Hazdra, CSc. podpis vedoucí(ho) ústavu/katedry	prof. Mgr. Petr Páta, Ph.D. podpis děkana(ky)

III. PŘEVZETÍ ZADÁNÍ

Diplomantka bere na vědomí, že je povinna vypracovat diplomovou práci samostatně, bez cizí pomoci, s výjimkou poskytnutých konzultací. Seznam použité literatury, jiných pramenů a jmen konzultantů je třeba uvést v diplomové práci.

.

Datum převzetí zadání Podpis studentky

© ČVUT v Praze, Design: ČVUT v Praze, VIC

Declaration

I declare that I completed the presented thesis independently and that all used sources are quoted in accordance with the Methodological instructions that cover the ethical principles for writing an academic thesis.

In Prague 22. 5. 2023 ....

Bc. Karolína Veselá

Acknowledgements

First, I would like to thank Ing. Vít Novák, CSc. and Ing. Zbyněk Šobáň, Ph.D. from the Institute of Physics for their attentive guidance and valuable advice during my theoretical and practical work on this thesis. I would also like to thank doc. RNDr. Jan Voves, CSc., for supervising this thesis. Second, I would like to thank my family and friends for their loving support during my studies at CTU.

Bc. Karolína Veselá

Title:
The Study of Antiferromagnetic Layers

Author: Bc. Karolína Veselá

Supervisor: doc. RNDr. Jan Voves, CSc.
Czech Technical University in Prague
Faculty of Electrical Engineering, Department of Microelectronics

Consultant: Ing. Vít Novák, CSc.
Institute of Physics of the Czech Academy of Sciences
Department of Spintronics and Nanoelectronics

Abstract:
This thesis explores the field of spintronics, focusing on the principles, materials, and working mechanisms of spintronic devices. The theoretical analysis sets the foundation for understanding the potential of antiferromagnet CuMnAs as a material for spintronics applications. In the experimental part of the thesis, a novel set-up is designed and implemented to measure the temperature dependence of CuMnAs resistivity. Systematic studies on different thin-film samples provide insights into the influence of sample thickness and other growth parameters on the critical temperature and conductivity. These experimental results deepen the understanding of CuMnAs behavior and its potential for spintronics applications.

Keywords: spintronics, antiferromagnets, CuMnAs, critical temperature

Název práce:
Studium antiferomagnetických vrstev

Autor: Bc. Karolína Veselá

Abstrakt:
Tato práce se zabývá oblastí spintroniky se zaměřením na principy, materiály a funkční mechanismy spintronických zařízení. Teoretická analýza tvoří základ pro porozumění potenciálu antiferomagnetického materiálu CuMnAs pro aplikace ve spintronice. V experimentální části práce je navržen a realizován nový experiment pro měření teplotní závislosti odporu CuMnAs. Systematický rozbor různých tenkovrstvých vzorků poskytuje poznatky o vlivu tloušťky vzorku a dalších růstových parametrů na kritickou teplotu a vodivost materiálu. Tyto experimentální výsledky prohlubují pochopení chování CuMnAs a jeho potenciálu pro aplikace v oboru spintroniky.

Klíčová slova: spintronika, antiferomagnety, CuMnAs, kritická teplota

Contents

1 Introduction to spintronics **1**

2 Possible working principles of spintronics devices **2**
2.1 Giant and tunneling magnetoresistance (GMR and TMR) 2
2.1.1 Hard disk drives 3
2.2 Spin-transfer torque and spin-orbit torque (SST and SOT) 4
2.2.1 Magnetoresistive RAM 4
2.3 Spin transistor 6

3 Materials for spintronics **8**
3.1 Diluted magnetic semiconductors 8
3.2 Antiferromagnets 9
3.3 Heusler compounds 10
3.4 CuMnAs 11
3.4.1 Electrical switching of CuMnAs 12
3.4.2 Quenching of CuMnAs 13

4 Molecular beam epitaxy **15**
4.1 Molecular beam epitaxy of CuMnAs 16

5 Transport properties of CuMnAs **18**

6 Experimental part **21**
6.1 Motivation for temperature measurement 21
6.2 Methods 22
6.2.1 Materials 22
6.2.2 Design of the sample 22
6.2.3 Sample preparation 23
6.2.4 Experimental set-up 24
6.3 Results 26
6.3.1 Calibration of the thermometer 26
6.3.2 Measurements of the resistance-temperature dependence of CuMnAs 26
6.3.3 Verification by SEM images 29
6.4 Discussion 30
6.5 Comparison of different CuMnAs samples 31
6.5.1 Comparison of different 20 nm GaP CuMnAs samples 31
6.5.2 Comparison of thicknesses of GaP CuMnAs samples 32
6.5.3 Comparison of different substrates 33
6.5.4 Final results 34

7 Conclusion **35**

Bibliography **36**

1. Chapter
Introduction to spintronics

Spintronics is a fairly new field of science that emerged in the 1980s with the discovery of giant magnetoresistance (GMR) and other findings concerning the spin of an electron in solids. Over the past 30 years, spintronics has evolved into a significant field of research focusing on new materials and electronic devices utilizing spin-polarized currents and other magnetic phenomena.

Spin is an intrinsic property of particles, including electrons, that gives them a fundamental angular momentum and magnetic moment. Spintronics can use two discrete states of the spin ("up" or "down") in reference to an applied magnetic field/magnetization of a material to carry information in the electrical circuit and be either another degree of freedom over the electric charge or be used alone. Combining standard microelectronics with spin-dependent effects, which will be discussed later in the thesis, brings out a new generation of devices with better performance qualities, the most relevant being nonvolatility, high processing speed, and low energy consumption.

In many materials, there is an equilibrium of the "up" and "down" states of the spin, and they do not affect the transport properties. To make a device spintronic, generating or manipulating a spin-polarized population of electrons is needed to tilt the spin equilibrium in a material. There are several methods to achieve that; the easiest one generates a spin-polarised current in a metal by passing the current through a ferromagnetic material. The material will become less polarized over time due to diffusion and other effects, causing a shortening of the spin lifetime, ways or materials that can prolong the spin lifetime are being researched (quantum dots, superconductors,...).

Recent research into spintronics uncovered the behavior of nanostructured magnetic systems subjected to electric currents, the association of charge and spin transport, and spin excitations in (non)magnetic systems [4]. The giant and tunnel magnetoresistance (GMR and TMR) effects and others are already used in industrial applications (2). However, there are still some challenges concerning the functionality and large-scale implementation. First, there is a high demand for magnetic materials grown with atomic-scale precision to exhibit the desired magnetic properties, such as high spin polarization and magnetic anisotropy. Many materials are multi-layered, and good lattice matching must be ensured. Choosing the suitable deposition method is, therefore, critical. Other future requirements are better scaling, optimization of a spin lifetime, decreased switching currents, and better implementation into complex circuits.

The research into new materials with better magnetic properties to fulfill these requirements encompasses ferromagnetic or antiferromagnetic thin films and heterostructures. One of the most promising groups of materials is half-metallic Heusler alloys, which will be discussed later (3.3).

2. Chapter
Possible working principles of spintronics devices

In this chapter, several of the magnetic effects related to the working of spintronic devices will be described with a follow-up description of examples of such devices that are either already on the market today or are currently being researched.

2.1. Giant and tunneling magnetoresistance (GMR and TMR)

GMR was discovered in the 1890s by Peter Gruenberg and also by Albert Fert and awarded by Nobel Prize in Physics in 2007. It was first observed as an effect in thin film structures composed of ferromagnetic and nonmagnetic layers in alternating order, e.g., Fe/Cr/FE trilayer. When a magnetic field is applied to these multilayers, a significant change in electrical resistance is observed, much bigger than the change in the known anisotropic magnetoresistance effect that happens in a single ferromagnetic material; this effect was therefore named giant MR.

The decrease in resistance, as shown in 2.1, happens when the magnetic moments of each magnetic layer align and the magnetization in the multilayer reaches a saturation state; the resistance is highest when the moments are antiparallel; this can be affected by an external magnetic field. This effect is based on the spin-dependent scattering processes that affect the spin orientation of the electrons as they pass through the multilayer superlattice, which has varying properties like bandgap energy. In other words, there is a difference in the scattering rates for electrons with different spin orientations leading to spin-dependent transport properties in the multilayer.

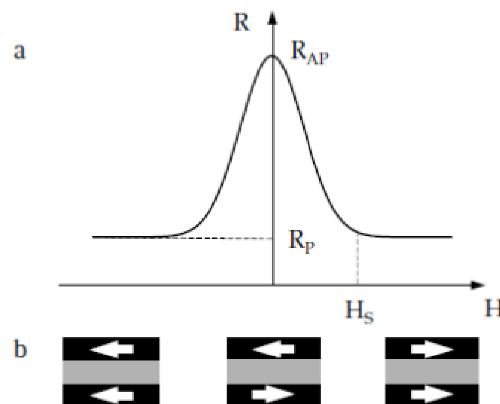

Figure 2.1: Schematic representation of the GMR effect. (a) Change in the resistance of the magnetic multilayer as a function of applied magnetic field, (b) the magnetization configurations of the multilayer at various magnetic fields. [6]

There are several types of the composition of the layers, the simplest one being a

multilayer formed by ferromagnetic and very thin nonmagnetic metallic layers creating stacks of 10 or more layers. To name one more type that is being used in many magnetic sensors, spin valve GMR is a good candidate. Its composition can be seen in 2.2, different from the previous multilayer; one of the ferromagnetic layers has a fixed orientation while the other is free and can react to changes from the applied magnetic fields. There are many more types of GMR, but as they are out of the scope of this thesis, they will not be mentioned here.

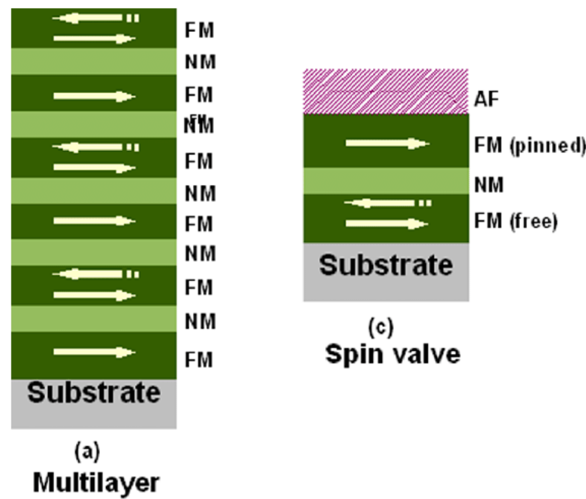

Figure 2.2: Different GMR structures (a) multilayer (b) spin valve. [5]

Tunneling magnetoresistance is an effect similar to GMR but based on a different physical mechanism. It involves again two ferromagnetic layers separated by an insulator. In this case, the insulator layer must be thin enough (typically a few nanometres) to act as a magnetic tunnel junction where electrons can tunnel from one FM to another. This quantum mechanical effect again enables the structure to switch between the states of high and low electrical resistance. The external magnetic field can affect both ferromagnetic layers individually. If their magnetization is in parallel orientation, the electrons will more likely tunnel through the junction than if it is antiparallel, causing the resistance to change accordingly.

2.1.1 Hard disk drives

The most significant technological applications of GMR and TMR are in the data storage industry; hard disk drives (HDDs) with read-heads based on these effects have been on the market for some time. Information in HDDs is encoded using magnetic domains with a specific orientation. Read-heads based on GMR use the spin valve multilayer. The free sensing layer of the spin valve changes its magnetic orientation while passing over the hard drive platter matching its orientation. As long as the free ferromagnetic layer has the same alignment as the fixed layer, the current flows through the structure with low resistance, being detected as a logical 1 by the computer. Once the orientation of the free FM layer changes to the opposite, the current gets much weaker, creating a logical 0.

The analogical principle applies to TMR read-heads, where the sensor is made of a stack of two ferromagnetic layers separated by the tunnel barrier. When a magnetic

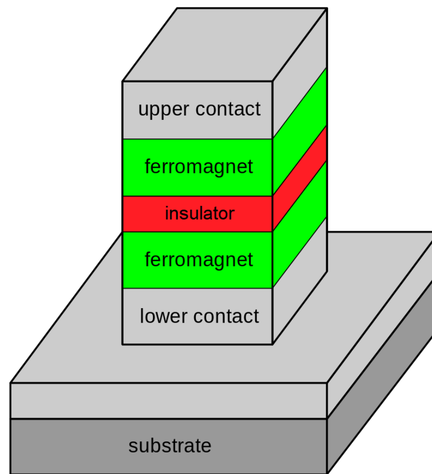

Figure 2.3: Schematic of magnetic tunnel junction. [7]

field from the data on the HDD platter is applied to the TMR sensor, the sensor's resistance changes due to the quantum mechanical tunneling of electrons through the insulating barrier. This resistance change can be measured to read the data.

Modern hard drives are using TMR for its better sensibility and speed over GMR read-heads; nonetheless, GMR HDDs are also widely used, the choice depending on the performance and cost requirements of each manufacturer.

2.2. Spin-transfer torque and spin-orbit torque (SST and SOT)

Spin-transfer torque is an effect where a spin-polarized current is used to change the magnetic orientation of a magnetic tunnel junction or a spin valve. Electric current is generally not polarized, having an equal number of both types of spin. The current can become polarized when run through a fixed magnetic layer; it can then transfer the spin angular momentum onto the second free magnetic layer, flipping its magnetic orientation. This effect can be used to store and manipulate digital information in non-volatile memory devices.

Spin-orbit torque is an effect describing the interaction of spin angular momentum with the orbital motion of the electron. SOT can be generated by passing an electrical current through a heavy metal layer, like Pt or Ta, with strong spin-orbit coupling. Spin-orbit coupling is a relativistic quantum mechanical phenomenon resulting from the electromagnetic interaction between the electric field generated by the electron's motion and the electron's intrinsic magnetic moment due to its spin. This effect causes the spins of electrons to become "locked" with their orbital motion, transferring the angular momentum further and creating a torque on an adjacent magnetic layer. Like SST, SOT is being studied for the development of magnetic memory and other logic devices, being also non-volatile and not needing an external magnetic field to work.

2.2.1 Magnetoresistive RAM

Magnetic random access memory (MRAM) is a promising non-volatile memory technology with data stored in magnetic domains. It was first developed in the 1980s and

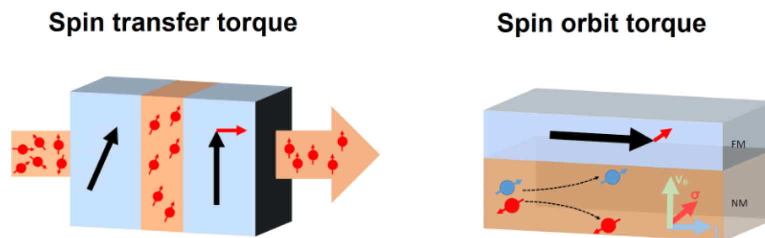

Figure 2.4: Possible set-ups for spin transfer torque device and spin orbit torque device. [22]

debuted on the market in 2006 as a 4 Mb product. MRAM has the potential to become the next dominant memory with its high speed and durability; however, so far, other types of RAMs, like DRAM and flash RAM, still have practical advantages over MRAMs.

A general memory device needs to have three key functions: storing, reading, and writing the information. Over the years, many different designs of MRAM have been researched, and usually, they perform these functions as follows: The storage of information is made possible by the magnetic retention properties of the magnetic anisotropy of a storage cell. The reading can be done by measuring the resistance of a current flowing through a magnetoresistive device. The writing operation involves the induction of a magnetic field onto the magnetic layer in the storage cell, or it can use the principle of STT.

The original working principle of MRAMs was based on the storage of magnetic elements, which can be formed by two ferromagnetic plates (one fixed and one free) separated by an insulating layer. The above-mentioned TMR and GMR effects have been used to create such MRAM memory either in the form of the magnetic tunnel junction structure or the spin valve structure, respectively. Here, the memory cell's resistance acts as the indicator of the direction of the magnetic moment stored in the free magnetic layer in the cell. However, these methods need a substantial current to operate in their performance window, not being able to meet the low-power demand and the scalability, which is limited by overlapping magnetic fields that could affect other cells in the storage unit.

MRAMs based on SST and SOT were developed to fix the previous shortcomings, needing less current to switch the memory and having greater speed of operation as well [9]. Moreover, SST MRAM does not need any external magnetic field to switch the magnetic moment, as this can be done by sending a current through the magnetic layers in the cell; this current can also be scaled, simplifying the fabrication process. Yet, there are still some challenges regarding the SST MRAM. Although the writing current is lower than in other types of MRAM, it is still relatively high, increasing the device's energy consumption as well. There are also issues with its reliability, as errors occur due to thermal fluctuations and other effects. SOT MRAMs are in a similar situation and will be mentioned more in ref.

As well as new technology, new materials are also being researched to achieve better MRAM properties. Antiferromagnetic media are being studied as an alternative to traditional ferromagnets, the main advantages being far shorter switching times, no effect on near particles, and immunity toward stray magnetic fields that could damage

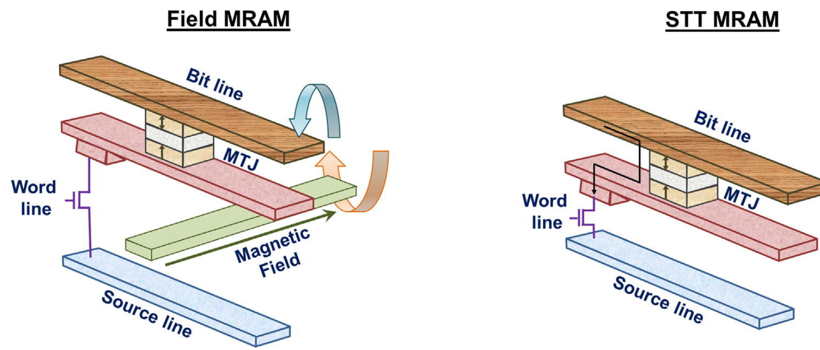

Figure 2.5: Comparison of the architecture of MRAM with a field induced switching and STT switching. [10]

data [11]. However, writing and reading antiferromagnetic memories is difficult due to their net zero magnetization; methods using SST, SOT, and other effects are being investigated.

2.3. Spin transistor

So far, the magnetic devices described above have been focused on storing data. There is also a possibility to process data not using the typical semiconductor devices like FETs but employing a spin field effect transistor (SFET). This concept dates back to 1990, when it was theoretically proposed by Datta and Das [15]. The potential of this device is to continue Moore's law in scaling down the size of transistors while also shrinking the power consumption.

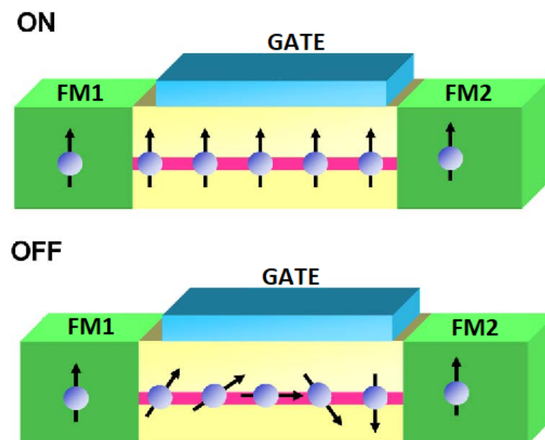

Figure 2.6: Operational principle of spin FET. [12]

Spin FET has a structure similar to FET but does not use the electrical current but the electron's spin as the operating force. The Source and Drain contacts are magnetic. The first magnetic contact injects electrons into the semiconductor material, the electrons being polarized in the ferromagnetic contact and keeping their initial spin as they move through the material. The other magnetic contact acts as a spin detector, letting only those electrons with matching spin inside. If both Source and Drain have the same spin orientation, the transmission is high, and the transistor is in the ON state. The Gate electrode here controls the spin rotation by means of the Rashba effect. Applying

voltage to the gate electrode creates an electric field with a magnetic component that would rotate the spins of electrons inside the SFET. In modern versions of SFET, the channel is made out of an SOI-active material, and the gate can control the spin-orbit interaction of the electrons [14]. Therefore biasing the Gate voltage can affect the number of carriers reaching the Drain, thus switching the state of the transistor between On and Off, as described in 2.6.

Although a working spin field effect transistor was already demonstrated (using a high-mobility InAs heterostructure) [14], SFETs are still far away from being used commercially. Each process, like spin injections or spin rotation, provides a different set of obstacles, and their working is far from the ideal principle described above. One of the creators of the spin transistor, Supriyo Datta, even argues that it seems more practical instead of trying to replace traditional FET to find ways to complement it. One such example is to use the resistance of a magnetic tunnel junction and combine it with FET to build a three-terminal device [15].

3. Chapter
Materials for spintronics

Spintronics devices mentioned in the previous chapter mainly use ferromagnets as the traditional building block. In 2.2.1, it was mentioned that antiferromagnets have the potential to replace ferromagnets in certain devices, being faster and more cost-effective. This chapter includes a brief description of the once-thought perspective ferromagnetic semiconductor materials and then shifts its focus to antiferromagnets, describing their basic properties. Lastly, the chapter singles out the primary experimental material of this thesis, CuMnAs, describing it as well as mentioning its impact on the spintronic up-to-date research.

3.1. Diluted magnetic semiconductors

In the search for semiconducting materials that would also have magnetic properties, a group of materials called diluted magnetic semiconductors (DMS) was discovered. They are nonmagnetic semiconductor alloys (GaAs, InAs,...) doped with naturally magnetic transition metals like Fe, Mn, or Cr. Such semiconductors can be prepared, for example, by MBE.

The percentage of doping directly affects the magnetic properties and the Néel temperature (critical temperaturefor of AFMs) or the Curie temperature (critical temperature of FMs). Manipulating these critical temperatures to be higher than room temperature is one of the goals in spintronics, as was previously mentioned. If implemented in electronic devices, DMS materials could be used for spin injections or can directly act as electrically controllable magnets.

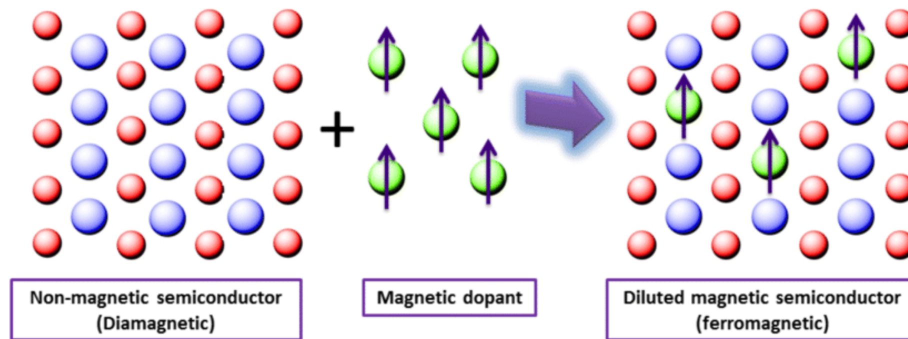

Figure 3.1: Mechanism for diluted magnetic semiconductors formation. [20]

One of the first DMSs created was GaAs doped with Mn, i.e. (Ga,Mn)As. If the doping of manganese is low (typically less than 10%), (Ga,Mn)As exhibits ferromagnetic behavior at low temperatures; however, when the Mn concentration is increased beyond a critical value, (Ga,Mn)As can act as an antiferromagnet due to the formation

of Mn-Mn antiferromagnetic clusters. Unfortunately, both critical temperatures are below the room temperature, in a range from 100 to 200 K [18]. Another type of DMS can be magnetically doped metal oxides such as ZnO, TiO_2, and others [19], which unfortunately also have a critical temperature below the room temperature.

3.2. Antiferromagnets

Antiferromagnets are materials with aligned magnetic moments in a regular, antiparallel pattern. Their magnetic order exists below a critical temperature; the critical temperature when the magnet stops being antiferromagnetic and becomes a paramagnet is called the Néel temperature, named after a Nobel prize winner who first identified the magnetic order of AFMs.

The crystalline structure of AFM is composed of an equal number of ions with spin "down" and spin "up". The simplest example of that can be a bipartite lattice that is formed by two sublattices, each with an opposite spin orientation, Figure 3.2, so, that the total magnetic moment of the structure is zero. The magnetic moments remain antiparallel, having zero net magnetization and keeping their position, even if a relatively strong external magnetic field is applied.

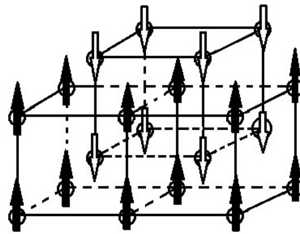

Figure 3.2: Schematic of antiferromagnetic crystalline structure of sub-lattices. [16]

Unlike the Curie temperature of ferromagnets, the Néel temperature of AFMs is typically above the room temperature, with the highest magnetic susceptibility at Néel temperature. Typical traditional groups of antiferromagnets are transition metal oxides (NiO, MnO) or transition metal alloys (FeMn). Because of their high Néel temperature and a wider variety of possible compounds compared to ferromagnets, they are promising for electronic applications. New groups of AFMs are being discovered, researched, and also artificially created. An example of these groups will be given below.

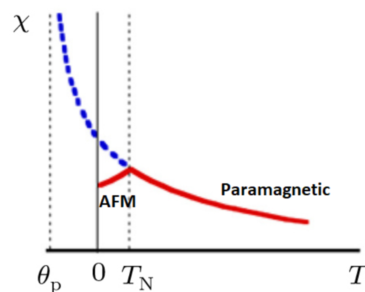

Figure 3.3: Temperature dependence of the magnetic susceptibility of antiferromagnetic solids. [17]

3.3. Heusler compounds

Heusler compounds are a promising group of materials for spintronic applications. This group includes XYZ compounds called half-Heusler and X_2YZ compounds called Heusler compounds, where X and Y are typically transition metals, and Z is a main group element. Together, these elements create intermetallic materials with unique properties, as the group includes semiconductors, antiferromagnets, half-metallic ferromagnets, superconductors, or topological insulators.

The class of Heusler compounds was discovered in 1903 by Fritz Heusler, and about 40 years ago, it became a point of interest in many fields, including spintronics, environmental technologies, and thermoelectrics. The unique feature of these materials is that their properties differ entirely from the properties of the single building elements. For example, Cu_2MnAl is a magnetic material even though none of the elements is magnetic. Figure 3.4 shows all the possible design combinations of the Heusler compounds, showcasing how huge the group of Heusler compounds could be.

Figure 3.4: Periodic table with overview on possible combinations of Heusler compounds. [1]

The properties of Heusler compounds depend strongly on their atomic order. The crystal structure is a face-centered cubic lattice with a ZnS-type substructure composed of two elements with the smallest difference in electronegativity. The whole crystal structure of both half-Heusler and Heusler compounds is seen in 3.5.

The XYZ elements are ordered according to their electronegativity, the most electropositive element being X. The overall number of valence electrons of compounds decides whether the compound is a semiconductor (with 18 valence electrons for half-Heusler or 24 for Heusler compounds) or metallic and magnetic. The bigger the valence electron number, the bigger the magnetic moment of the material and the Curie/Néel temperature, which is well above the room temperature for many of these compounds.

Heusler compounds are currently intensively studied for their potential to be the new material in spintronics devices such as magnetic tunnel junctions, GMR, and spin-injections devices. The tunability of their properties brings the opportunity to use them in energy conversion and storage.

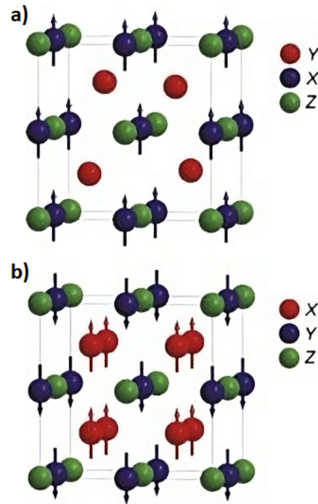

Figure 3.5: Crystal structure of (a) half-Heusler compound, (b) Heusler compound. [1]

3.4. CuMnAs

In a search for a good antiferromagnetic material with high Néel temperature that would fit the needs of a functional spintronic device, the scientists of the Department of Spintronics and Nanoelectronics at the Institute of Physics of the Czech Academy of Sciences discovered a new material, tetragonal phase of CuMnAs [21]. CuMnAs is from the family of half-Heusler compounds but with a unique crystal structure.

The tetragonal structure of CuMnAs, as shown in the 3.6, has an equal amount of neighboring Mn atoms with spin "up" and spin "down". This tetragonal shape of the crystal is anisotropic, meaning that it removes frustration in the nearest-neighbor magnetic coupling, increasing the Néel temperature of the compound. Mn sublattices with the opposite signs are mutually inversion-symmetric, which has important consequences for the magnetic behavior, as will be shown later.

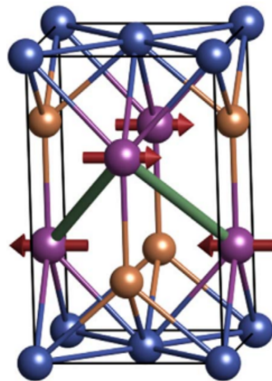

Figure 3.6: Crystal structure of tetragonal CuMnAs with Mn nearest neighbors highlighted in green. [21]

CuMnAs can be prepared by molecular beam epitaxy. It can be grown as a thin film on III-V semiconductor substrates like GaAs and GaP and also on Si substrates. The production process is described in more detail in the next Chapter 4. CuMnAs was found to have a high crystalline quality and chemical order [21]. Additionally, prepa-

ration by a conventional MBE system makes it possible to combine it with established semiconductor heterostructure technologies.

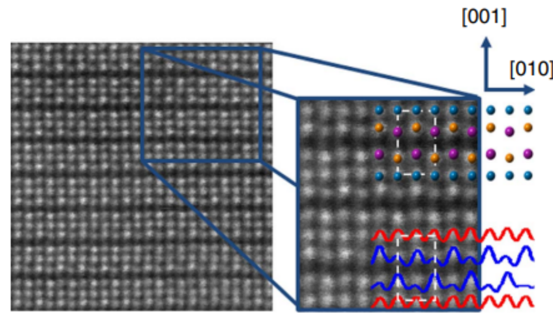

Figure 3.7: STEM image of CuMnAs along the [100] direction. [21]

3.4.1 Electrical switching of CuMnAs

As was previously mentioned, ferromagnetic memory devices have the disadvantage of their data being erased by perturbing magnetic fields either from the outside or inside. The AFM MRAMs would be immune to this; additionally, they have faster spin dynamics and a broad range of materials keeping their AFM order at room temperature. However, due to their overall zero net magnetization, antiferromagnets are hard to control using external magnetic fields. Using relativistic quantum mechanics can, in fact, generate current-induced internal fields making it possible to write and read information from an AFM. This was demonstrated on CuMnAs thin-film device [23], and will be briefly described in this section.

The most advanced FM MRAMs use the spin-transfer torque effect for electrical writing by injecting spin-polarized carriers from a fixed FM layer to a free FM layer. In AFMs, simple spin-polarized current can not exist because of the alternating magnetic order. However, the effect of the spin-orbit torque leads locally to alternating spin-polarization even in the AFMs. If, moreover, two spin sublattices of the AFM form inversion partners, this local polarization gives rise to an effective magnetic field which may reorient the magnetic order of the whole AFM crystal.

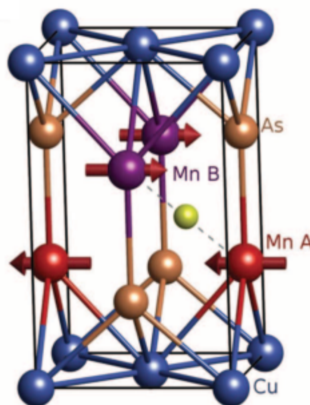

Figure 3.8: CuMnAs crystal structure and AFM ordering. The full CuMnAs crystal is centrosymmetric around the interstitial position highlighted by the green ball. [23]

In CuMnAs, two Mn sublattices indeed form inversion partners creating the described local nonequilibrium spin polarizations of opposite signs, which can be used to electrical switching of the magnetic orientation. The switching is realized by current pulses applied along two orthogonal in-plane cubic axes of CuMnAs, as shown in 3.9. The writing into the CuMnAs device was done at a temperature of 273 K and by a current of $4 \cdot 10^6 \mathrm{Acm}^{-2}$, which is a lower current than the one typically used in SOT switching of FM.

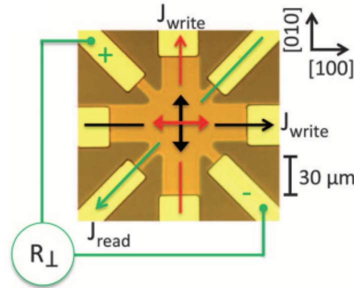

Figure 3.9: Optical microscopy image of the CuMnAs memory device and schematic of the measurement geometry. Bright yellow areas are Au contact pads. [23]

Due to the CuMnAs structure, writing current pulses in one direction increase the amplitude of the readout signal in one direction, and pulsing in the orthogonal direction increases the perpendicular signal. Reading is realized by measuring the anisotropic magnetoresistance of the device in the direction tilted by 45° against the writing current direction (which is the direction of the maximal signal). Hence the AFM memory can be read and written by current-induced fields, and its data are kept even in the presence of strong magnetic fields.

3.4.2 Quenching of CuMnAs

Another research into CuMnAs properties found interesting behavior of the AFM magnetic domains while quenching the CuMnAs thin film using electrical or optical pulses [24]. This research was done in order to look for new ways to increase magnetoresistive signals, which are generally weak, not only in AFMs.

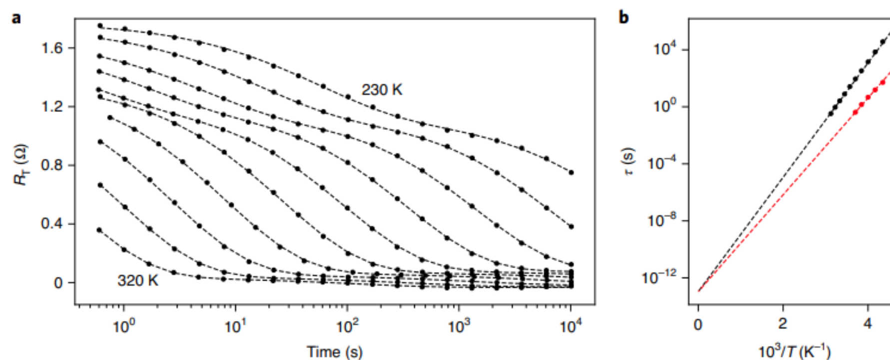

Figure 3.10: (a) Time dependence of the relaxation of the switching signal in CuMnAs for different temperatures. (b) Relaxation times inferred from fits in (a) as a function of the inverse temperature. [24]

By applying pulses with a current density over 10^7 Acm^{-2} or ultrashort optical pulses, CuMnAs is brought to the vicinity of its critical temperature and, therefore, its magnetic transition point. The antiferromagnetic state is then fragmented into a large number of small domains, which get frozen (quenched) when quickly cooled down. These changes are deterministic and reversible and can be measured by simple longitudinal resistance. In Figure 3.10, the relaxation immediately following the switching impulse can be seen. This relaxation contains two main exponential components, corresponding to two different relaxation times. The faster component leads to room-temperature relaxation times in the range of 10 ms, the slower 10 s. However, there is yet another much slower relaxation process not captured in Figure 3.10 with a relaxation time of up to several hours. The exact physical phenomena behind this relaxation have never been experimentally studied and remain unclear.

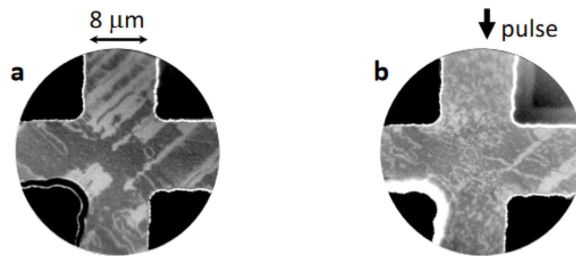

Figure 3.11: (a) Domain structure of 50 nm CuMnAs on GaP observed by XMLD-PEEM (b) the same domain structure ofter applying 500 μs current pulse of amplitude $1 \cdot 10^7$ Acm^{-2}. [24]

4. Chapter
Molecular beam epitaxy

Molecular beam epitaxy (MBE) is one of the most precise epitaxy methods used for the growth of thin-film crystals. The origins of MBE can be traced back to the 1950s, and since then, the method has been used for manufacturing semiconductors and other materials for magnetical or optical applications. MBE is now recognized as one of the fundamental methods for researching and developing nanotechnologies.

The epitaxial growth of MBE takes place in an ultra-high vacuum chamber at usually high temperatures. The desired materials for deposition are pure elements kept in separate sources, usually of the quasi-Knudsen effusion cells type. These cells can be heated in order to vaporize the elements. When heated, the released atoms or molecules are transported as a beam onto the substrate in the vacuum chamber, where they are deposited. Controlling the temperature of the effusion cells regulates the rate of material being evaporated, and controlling the substrate temperature affects the deposition rate. The term 'beam' means that evaporated atoms or molecules on their way to the substrate do not interact with each other or with the vacuum-chamber gases due to their long mean free paths. By varying the source materials, it is possible to create one atomic layer at a time, creating nanostructures with precisely controlled compositions.

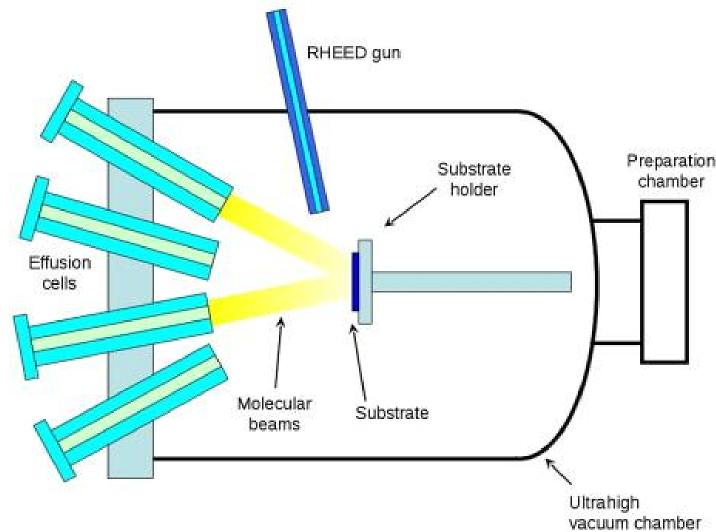

Figure 4.1: A simple sketch showing the main components and a schematic layout of the main chamber in MBE system. [30]

During MBE operation, reflection high-energy electron diffraction (RHEED) is often used to monitor the crystal layers' growth. A computer controls shutters in front of each effusion cell, allowing precise control of the thickness of each layer down to a single layer of atoms. Such control has allowed the development of structures where the electrons can be confined in space, creating nanowires, quantum wells, or even quantum dots.

The high crystalline quality of materials grown by the MBE process usually requires a slow deposition rate, typically in units of nm per minute. The systems of MBE are

also costly and, therefore, unsuitable for extensive industrial utilization. However, MBE plays a crucial role in many research and development laboratories worldwide thanks to its high precision and defect-free deposition and the wide scope of materials that can be prepared by it.

4.1. Molecular beam epitaxy of CuMnAs

As was mentioned above, many new magnetic materials are being prepared by MBE, including the antiferromagnetic tetragonal CuMnAs, which is the main material of investigation in this thesis. One of CuMnA's favorable properties is the high degree of structural compatibility with common semiconductor materials such as GaAs, GaP, and Si. A successful epitaxy of CuMnAs was achieved on all three types of substrates (GaAs, GaP, and Si). The CuMnAs thin film grows on these substrates under 45° in-plane rotation, as can be seen in Figure 4.2 (a). The typical sample structure is shown in Figure 4.2 (b), where first, a buffer layer is grown onto the substrate to improve the quality of the semiconductor-CuMnAs interface. Then an Al capping layer is deposited onto the top of the CuMnAs layer as protection against oxidation; the Al alone oxidizes in the air, forming a stable AlO_x protective layer.

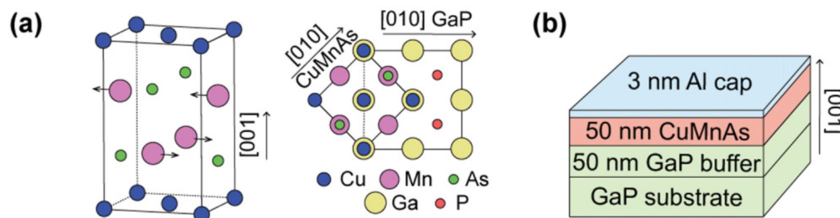

Figure 4.2: (a) Model of tetragonal CuMnAs unit cell. (b) Sketch of the cross-sectional structure of MBE prepared samples. [28]

The optimal growth temperature for CuMnAs samples was determined to be in the window from 190 to 260 °C with best results around 220 °C. During the growth, the substrate temperature is determined by measuring the optical absorption edge of the semiconducting substrate. Thus, layers of thickness up to about 50 nm can be reliably grown. During the initial stage of the growth, an effect of island formation can be observed in, e.g., the AFM microscope. These patterns gradually reduce until a continuous flat, hole-free surface is formed at around 20 nm. These characteristics are similar for all three kinds of substrates.

CuMnAs on GaP was found to have the most smooth surface out of the three substrates, while GaAs and Si substrates led to a significantly higher surface roughness of the CuMnAs thin film. This is not surprising as the GaAs has a large lattice mismatch with CuMnAs, and Si has a nonpolar surface. To investigate the interface of the AFM and substrates more closely, STEM images of these interfaces were obtained, as shown in Figure 4.3. In the case of GaP, a pristine interface can be seen with only a few disturbances. The GaAs interface is, on the other hand, disturbed by arrays of misfit dislocations caused by the substrate-film mismatch. The Si interface shows the highest disturbance, having multiple crossing slip dislocations, as shown in Figure 4.3 (c).

Obviously, the defects caused by the different substrates might affect the magnetic properties of CuMnAs. For example, atomically sharp magnetic domain walls have been

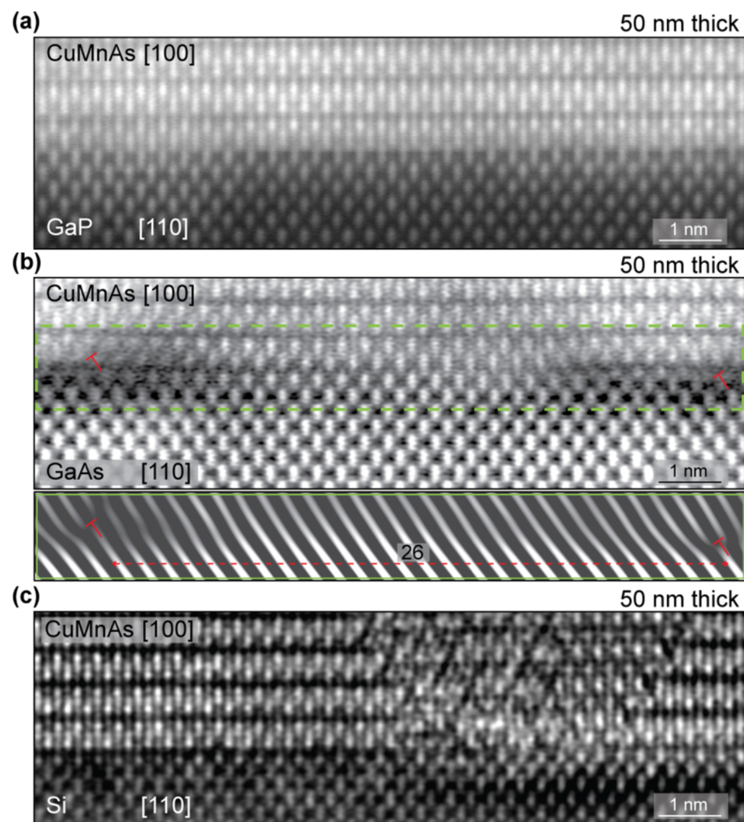

Figure 4.3: (a) HAADF-STEM micrograph of the interface between CuMnAs and GaP, (b) GaAs with the area selected in green high-lighting misfit dislocations, and (c) Si. [28]

experimentally found for the first time in this material. However, a detailed theoretical study of these effects is still missing.

5. Chapter
Transport properties of CuMnAs

It was already demonstrated that CuMnAs is a very promising material for spintronic applications. And while there have been publications on its transport properties, they mainly focused on effects directly related to magnetism, such as magnetoresistance or electrically induced magnetic switching. As for the electrical transport properties, there are still many gaps in the literature. This chapter will provide an overview of what has been known so far and will showcase the limitation of these findings as well as the motivation for the following experimental part of the thesis.

The electrical conductivity of CuMnAs is, in a way, similar to metals highly sensitive to temperature: with the rising temperature, the resistance of CuMnAs increases. Measurement of this dependence into low temperatures where CuMnAs keeps its magnetic order has been done before and can be seen in Figure 5.1. The resistivity at 4 K is about 90 $\mu\Omega$ cm rising to about 160 $\mu\Omega$ cm at 300 K. Residual-resistivity ratio of about 2 can also be observed, indicating a decent crystal quality of the tetragonal CuMnAs with few impurities and defects.

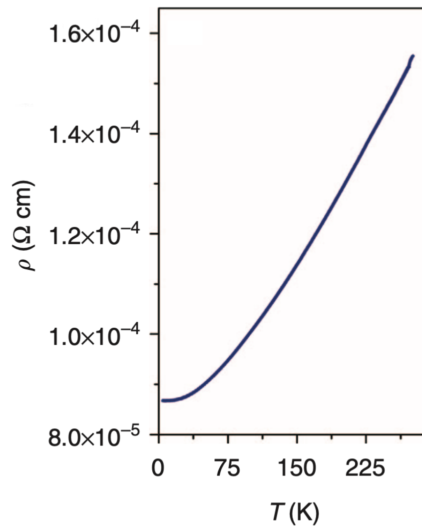

Figure 5.1: Temperature dependence of resistivity of CuMnAs. [21]

In contrast to low temperature, the high-temperature dependence of CuMnAs resistivity has been only rarely mentioned in the literature, and no systematic study has been published. Nevertheless, important physics occurs in this temperature range, particularly close to the critical point, which can be expected to show up in the resistance.

There have been only a few attempts to measure the critical temperature of the thin film CuMnAs. In one of them, a 500 nm thin film CuMnAs was subjected to neutron diffraction. The measurement has been done in (100) and (001) crystal planes in a range of different temperatures. The measured intensity of neutron diffraction peaks was put into a context with temperature, as seen in Figure 5.2. The temperature dependence

was then suitably fitted, and the Néel temperature was determined to be (480 ± 5) K.

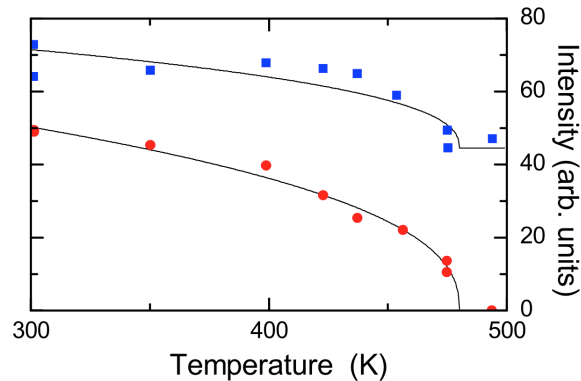

Figure 5.2: Temperature-dependent fitted intensities of the neutron diffraction peaks for the (100) reflection (circles) and the (001) reflection (squares). [25]

The purely magnetic reflection (100) (red circles in 5.2) shows a decline with increasing temperature, as expected from the magnetic order's dependence on the temperature. However, critically observing the results in Figure 5.2, the fitted function shows some uncertainty, not being quite precisely fit, giving relatively wide space for the exact determination of the Néel temperature, maybe even more than ± 5 K range.

Another attempt at high temperature measurements was made with an on-heater Pt100 sensor, where CuMnAs resistance was measured by a commercial four-point probe on an unpatterned sample surface. This experiment was done at the Institute of Physics. However, the final results were confusing. Observing the Figure 5.3, one can notice various instabilities and changes in resistance. It is unclear if these changes reflect the magnetic behavior of the antiferromagnet or if they are just artifacts caused by inadequate electrical contacts between the probe and the sample or imperfect thermal contact between the heater and the sample. Another question focused on the observed open loops, where it could not be decided if they reflected a true hysteresis in the resistance or if they were caused by a delay between the sample and the temperature sensor.

The main issue with most high-temperature measurements is its experimental setup. It must ensure homogenous heating over the whole sample. It must consider the delay caused by heat transfer from the source onto the sample and the decrease in the temperature along the way and it must ensure stable electrical contacts. To prevent oxidation of the sample, there must be at least a high vacuum in the heating chamber as well. Moreover, if the material turns out to be prone to annealing, the experiment must be repeated several times to capture this effect, too.

In the experimental part of this thesis, a new experimental set-up is designed, suitable for high-temperature measurements of CuMnAs. In the rest of the work, this set-up will be applied to a systematic study of temperature-dependent transport phenomena in thin-film samples of the CuMnAs material. In particular, the determination of Néel temperature will be attempted.

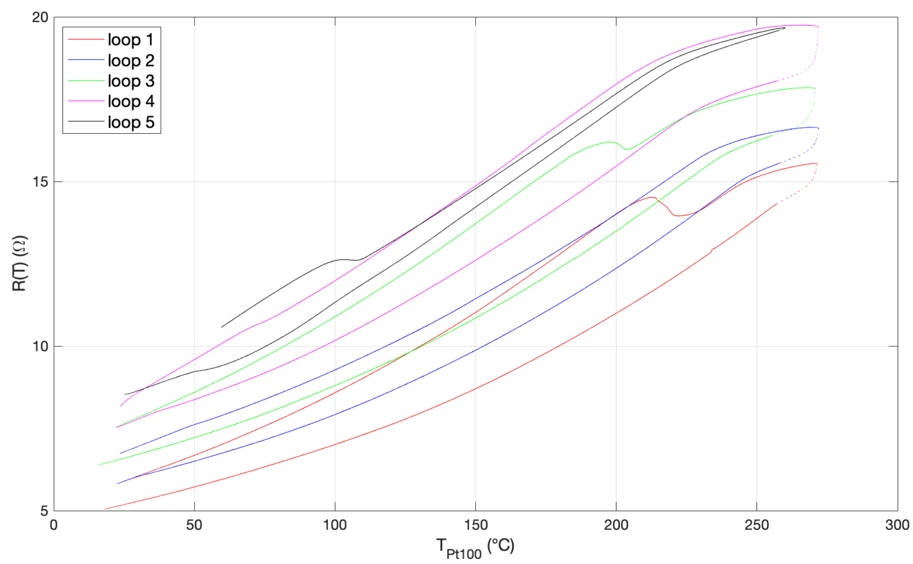

Figure 5.3: Previous temperature measurements done by ramping between low and high temperatures.

6. Chapter
Experimental part

Experimental part of this thesis focuses on measuring the transport properties of thin antiferromagnetic film of CuMnAs. It follows up the previous unsuccessful measurements of its transport behavior at high temperatures between 200 and 300 °C and comes up with an innovative method of measuring the temperature dependence of resistivity of a sample in a vacuum chamber. For more precise temperature measurements, a platinum thermometer is sputtered right onto the surface of the CuMnAs sample, which is prepared by means of laser lithography.

The measured material comes from the Department of Spintronics and Nanoelectronics laboratory at the Institute of Physics of the Czech Academy of Sciences, where it was first prepared and is still grown by the highly-precise method of Molecular beam epitaxy. The presented experiment was done in cooperation with this institution; it took place in their laboratories, including the clean-room laboratory, and under the supervision of Ing. Vít Novák, CSc.

6.1. Motivation for temperature measurement

Coming up with a precise method for measuring the sample temperature was one of the critical parts of the experimental design. First, the sample was heated by a heater element consisting of a tungsten wire encapsulated in a thin ceramic plate. At first, the temperature of the sample was measured by two Pt100 sensors: one glued to the bottom of the heater and another one glued to the same chip carrier that would be holding the CuMnAs sample on top of the heater in the chamber. Both sensors were used to measure the temperature simultaneously while the heater was ramping from room temperature to about 250 °C, waiting there and then going back.

In Figure 6.1 (a), a clear difference can be seen between the readings of the two sensors. Figure 6.1 (b) shows a false hysteresis that is, in fact, created by the time delay between the two sensors. To further demonstrate the uncertainties in determining the correct temperature, the tungsten wire of the heater can also be used as an independent third sensor due to its resistance changing linearly with the temperature. It is possible to scale this resistance to any of the Pt100 sensors leading, however, to a third alternative time-shift of the reading (Figure 6.1 (c)).

These findings showcase that the only reliable temperature measurement method during varying temperatures is putting the sensor directly on the CuMnAs chip. This method requires the preparation of the CuMnAs film and the sensor lithographically, which was a challenging endeavor.

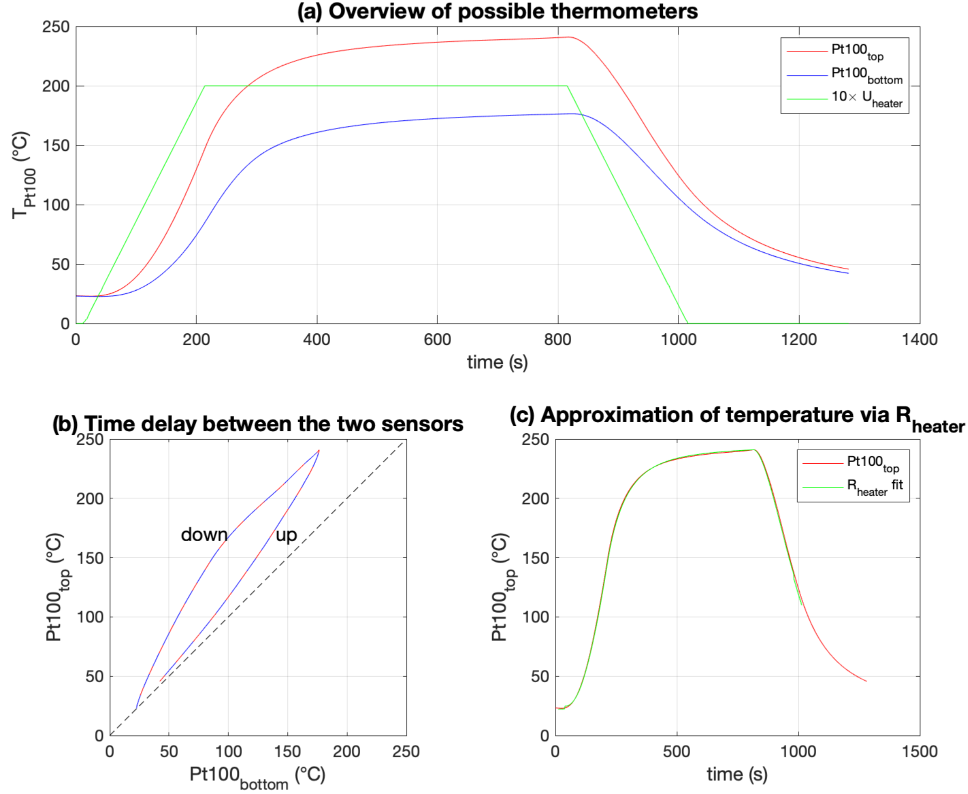

Figure 6.1: Graphs illustrating the difficulties of temperature measurement by different temperature sensors.

6.2. Methods

6.2.1 Materials

CuMnAs thin films were prepared by MBE on three different types of substrates: GaP, GaAs, and Si. For the sake of comparison, these samples grown on different substrates had identical thicknesses of 20 nm. GaP substrate samples with 10 nm and 50 nm were also prepared to measure the impact of the thickness parameter on the temperature dependence. Some samples were prepared in different crystallographic orientations, too. The follow-up table 6.1 shows an overview of chosen samples used in the experiment together with their basic properties.

6.2.2 Design of the sample

The structure of the CuMnAs sample was designed using a bar-shaped geometry having two current contacts at the ends and two pairs of contacts along the sides, see Figure 6.2 (b). The main current channel of the bar structure has the dimension of 5 x 110 μm. To examine whether the sample exhibits anisotropic properties, the design of the chip contains several structures with four different directions of orientation. The design also includes a thin layer of platinum created to operate as a thermometer. The platinum channels have three widths, 3, 3.5, and 4 μm, and are prepared to be measured by the

Name	Substrate	Thickness [nm]	Orientation
C234#6	Si	20	(100)
C236#10	GaAs	20	(100)
C236#13	GaAs	20	(100)
C247#9	GaP	20	(100), (110)
C254#7	GaP	10	(100)
D205#1	GaP	20	(100), (110)
D206#9	GaP	50	(100)
D210#2	GaP	20	(100)

Table 6.1: Overview of chosen CuMnAs samples with their specific properties.

four-point method. To spare the fabrication time, the final chip consists of four almost identical parts that can be cut apart and measured separately, Figure 6.2 (a).

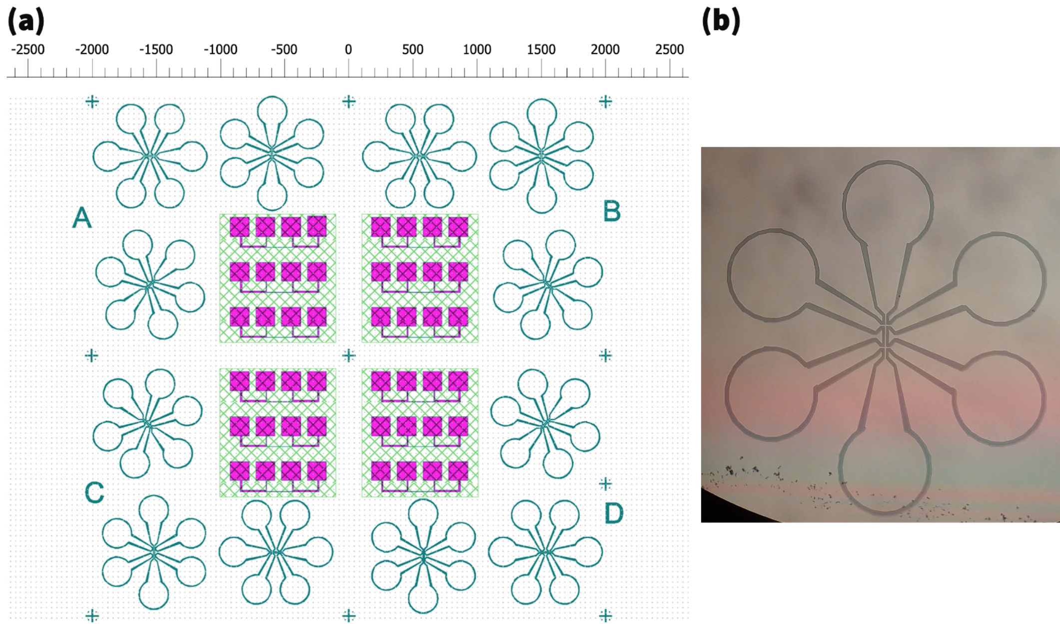

Figure 6.2: (a) Design of the CuMnAs chip, including platinum thermometer (pink color). The dimension scale provided in the diagram is in micrometers (µm). (b) Detail of the bar geometry of one CuMnAs structure.

6.2.3 Sample preparation

The design was transferred onto the chip by means of laser lithography. The lithography process was done in a clean room of class 1 000 using Microwriter ML3 Pro by Durham Magneto Optics. The laser imagining was done in two phases; a positive photoresist was used in each. In the first phase, the designs of CuMnAs structures were patterned, as well as the rectangular fields for the future Pt sensors.

After the film developing and etching in the first lithographic phase, where the CuMnAs layer was completely etched-off, the rectangular fields with removed CuMnAs layer were used in the second lithography step in order to fabricate the Pt thermometer. After developing the exposed photoresist, the sample was transferred into a sputtering

machine, where an about 50 nm thick layer of platinum was deposited onto the surface of the sample. After the lift-off of the redundant platinum from the surface, the chip was ready to be transferred into the next step of the preparation process, see Figure 6.3.

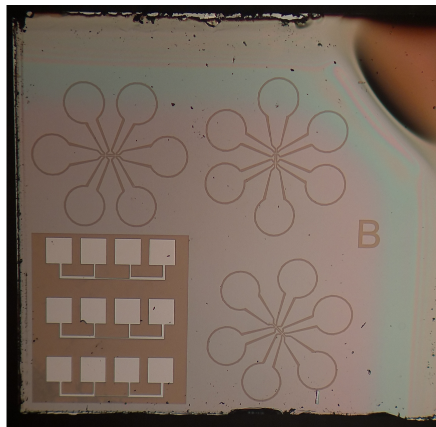

Figure 6.3: Quarter of the CuMnAs chip with platinum thermometer, covered with resist for protection.

A chosen part (a quarter) of the chip was cut out and glued to a corundum ceramic chip carrier in order to distribute the heat uniformly across the whole measured sample while also isolating the sample electrically.The chip carrier has a size of 10 x 10 nm. Using a bonder machine leads between the microscopic contact pads on the chip and the macroscopic contact pads (made of copper) on the chip carrier were made using thin aluminum wires with a diameter of 30 μm. Thicker copper wires (diameter of 200 μm) were then attached to the ceramic chip carrier, see Figure 6.4.

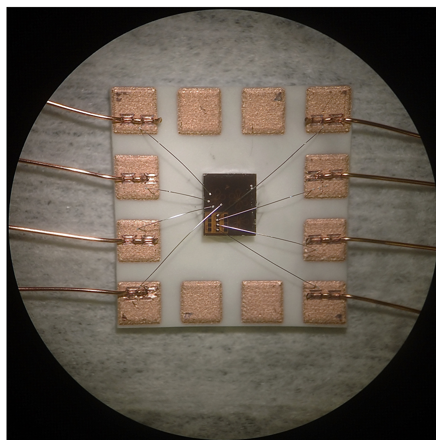

Figure 6.4: Quarter of the CuMnAs chip is glued to the ceramic chip carrier with wire-bonded contacts.

6.2.4 Experimental set-up

The CuMnAs chip was measured in a small metallic vacuum chamber at the Institute of Physics. The chamber accommodates a ceramic heater element with a tungsten wire that provides resistive heating. The chip carrier with the bonded chip is placed onto

the heater and is fixed by two stainless-steel springs. Copper wires leading from the chip carrier are soldered to fixed contacts next to the heater, and the signals are lead through a vacuum-sealed connector out of the chamber.

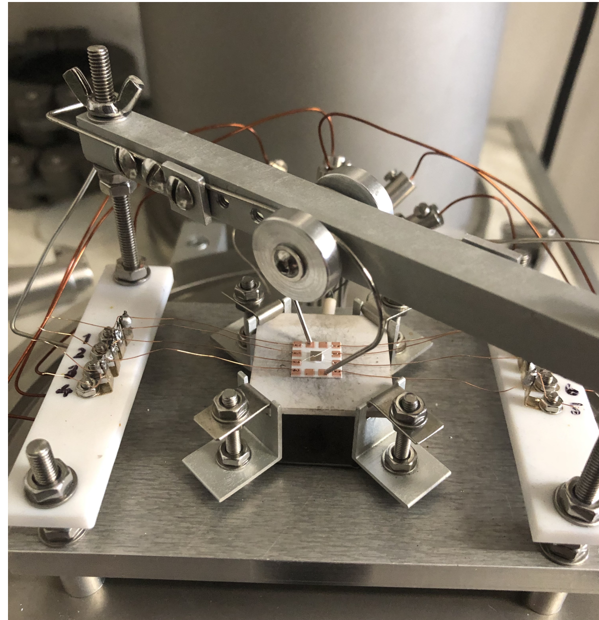

Figure 6.5: The inside of the heating chamber with the heater element (larger ceramic plate in the center of the picture, fixed at the corners and the chip-carrier with the chip on the top pressed down by two steel springs).

The heating chamber was evacuated using a combination of a turbomolecular pump and a roughing scroll pump, resulting in a high vacuum. The pumping system kept a vacuum pressure of the order of 10^{-6} mbar during the measurement. The heating source of the chamber was connected to a voltage source with a software-controlled output voltage between 0 and 31 V. Additional current sources Keithley 2400 and voltmeters Keithley 2000 were used to measure the resistance of the CuMnAs thin film and the platinum thermometer. The current through the CuMnAs sample was typically 30 μA; the current through the platinum sensor was adjusted to 100 μA.

Figure 6.6: The sealed heating chamber. The vacuum pumps are connected by a bellow from the bottom.

6.3.1 Calibration of the thermometer

The on-chip platinum thermometer was tested by a ramping procedure of the heater. It consisted of slowly increasing and decreasing the heater current and, thus also, the temperature. During the ramping, the temperature was measured by two sensors. As the first sensor, the heater-element resistance scaled to the top Pt100 sensor was used (see also 6.1) to measure the stabilized (or only slowly varying) values around the temperature extremes; this reading is labeled T_h. In place of the second sensor, the resistance of the on-chip Pt element was measured, which can also be linearly scaled to temperature; this reading is labeled T_{Pt}.

As an initial guess, the scaling constants were chosen to fit together T_{Pt} and T_h in the first period of the temperature ramping; see a second panel in Figure 6.7. Two effects can be immediately observed. First, at the given ramp rate, T_{Pt} is delayed by approximately 100 s after T_h; this has been expected and can be straightforwardly explained. Second, after heating to a higher temperature, the resistance of the Pt changes, and T_{Pt} starts to deviate from T_h. This annealing effect is known and typical for most metallic thin films [26]. The Pt annealing saturates at a high temperature after a sufficiently long time; unfortunately, the CuMnAs sample is also exposed to a heat treatment during that time. Therefore, the following calibration procedure is applied to the T_{Pt} to correct the initial annealing effect.

The sensor temperature T_{Pt} is fitted to T_h in each time interval where T_h remained below 150 °C, i.e., always around the temperature minimum. At this temperature, no annealing effect is observed. The resulting scaling constants in these time intervals and also in times immediately before and after these intervals up to the adjacent temperature maxima (red curves in the lower panel of Figure 6.7 (a)) are used in the calibration. As can be seen, around each temperature maximum, calibrations from the left and right may differ, reflecting the uncertainty in the temperature during the first heatings before the annealing process saturates. The evolution of the Pt calibration function and its final saturation is shown in Figures 6.7 (b) and (c).

6.3.2 Measurements of the resistance-temperature dependence of CuMnAs

A typical example of the dependence of resistance on temperature and the annealing effect relating to it is depicted in Figure 6.8. The heating process is represented by the red lines, while the consecutive cooling of the sample is shown by the blue lines.

At first, the heating curve of CuMnAs exhibits a relatively flat trend, with the resistance monotonously increasing as the temperature rises. Below 280 °C, no noticeable annealing effect is observed, and there are no signs of hysteresis/bistability or any distinct feature around the expected Néel temperature. However, upon annealing the sample at higher temperatures, a significant increase in resistance is observed, accompanied by an appearance of a clear hysteresis between the heating and cooling lines. Notably, all annealed measurements exhibit a distinct maximum on the derivative line when dR/dT is calculated.

To illustrate the progress of annealing, values of resistance of several selected temperatures are plotted against the annealing time in Figure 6.9. It is seen that at 280 °C,

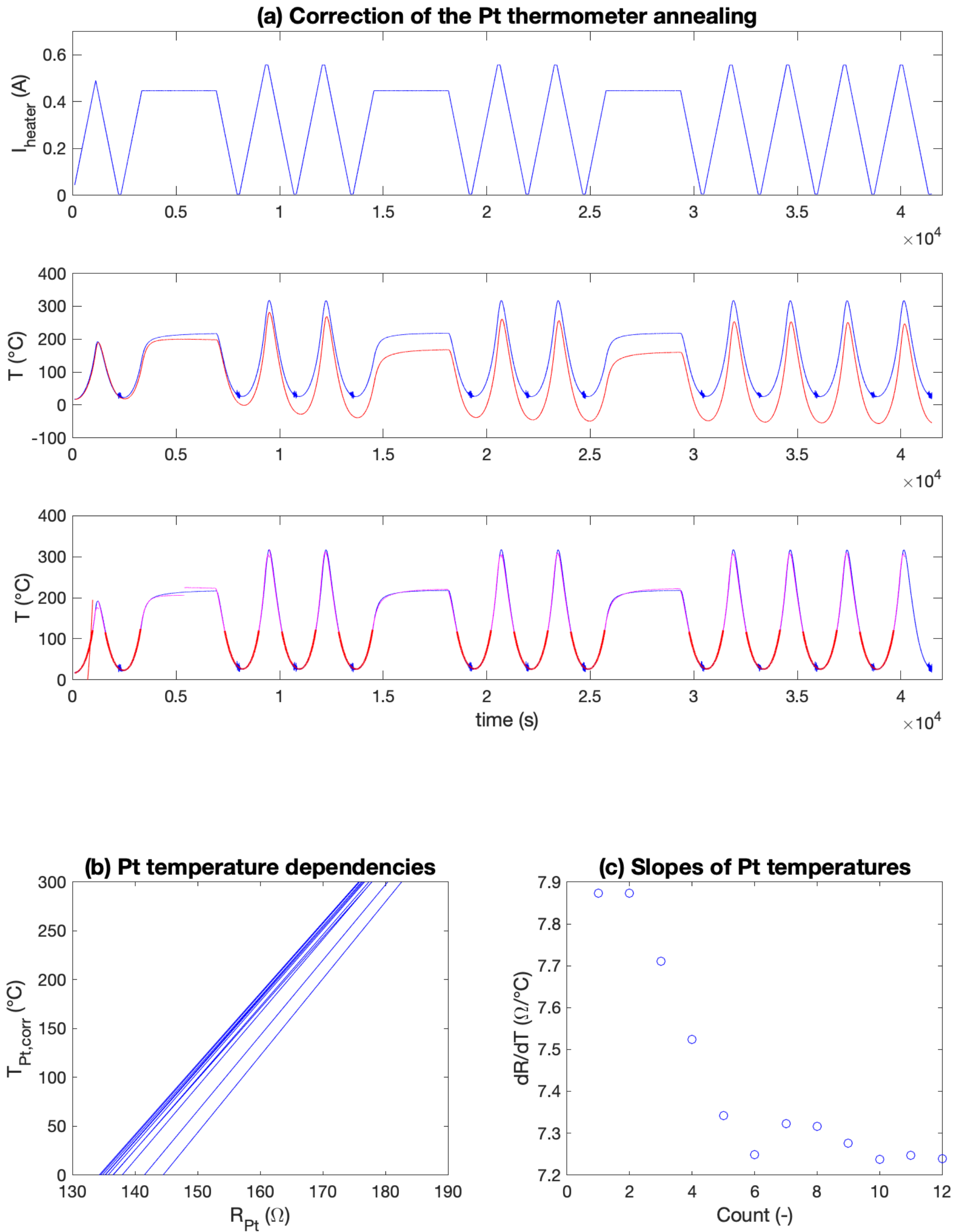

Figure 6.7: Illustration of the calibration process: blue curves in (a) represent the current (upper panel) and temperature (middle panel) of the heat source while red curves represent T_{Pt} that is being calibrated. In (b) the development of the calibration functions is shown. Their slow saturation is also shown in (c) using slopes of these calibration functions.

the annealing saturates, and the hysteresis develops after approx. 200 min. At further

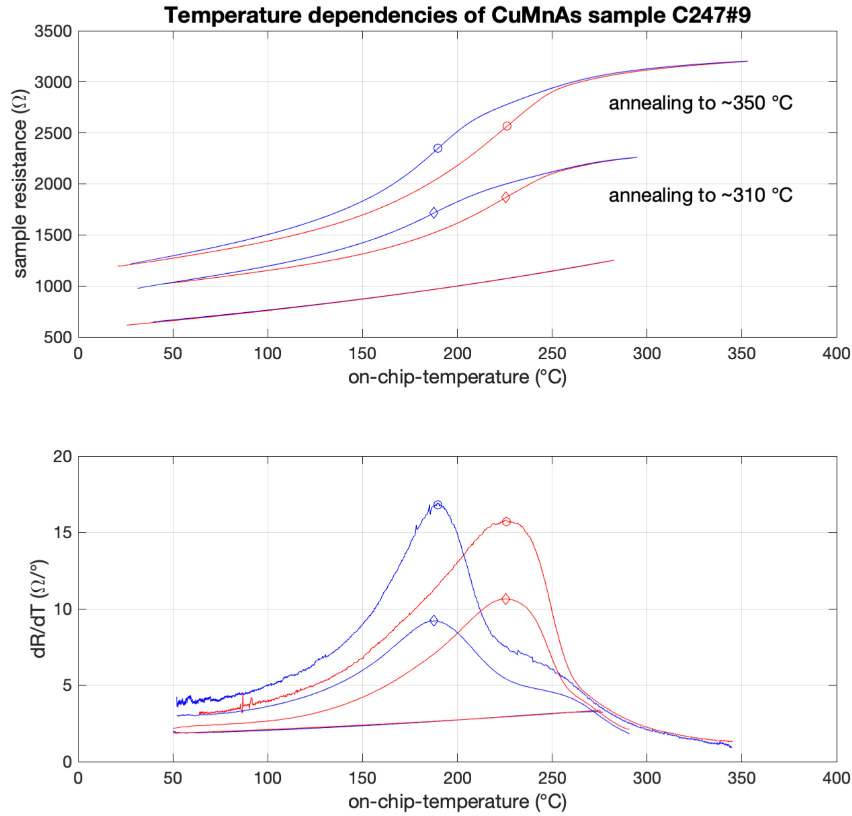

Figure 6.8: Upper panel: temperature dependence of a 20 nm CuMnAs film on GaP substrate. Lower panel: temperature derivative dR/dT of the resistance. Position of peak in dR/dT are marked also in the upper panel.

increased temperature, the annealing sets on again but quickly saturates.

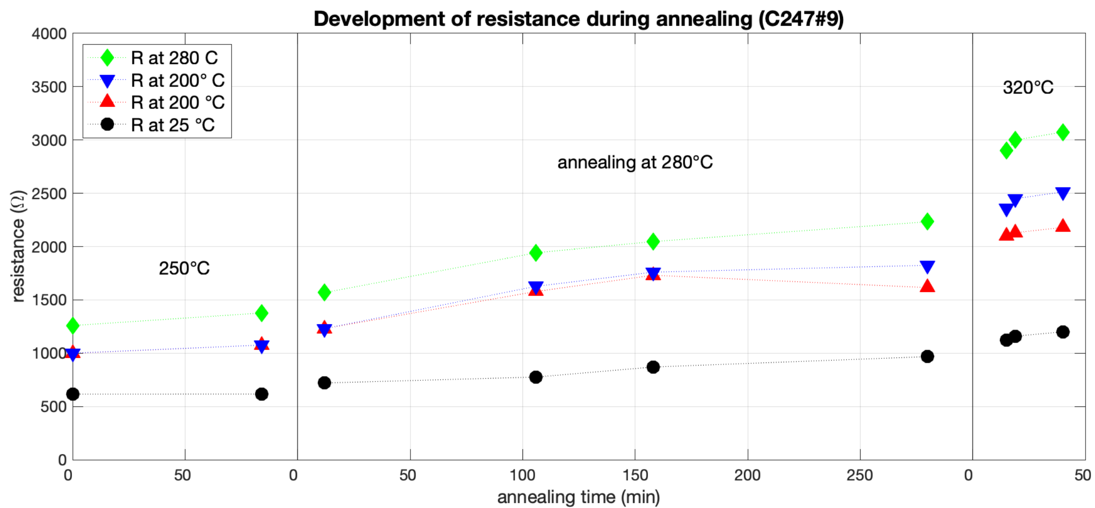

Figure 6.9: Development of resistance during annealing, red marks represent increasing in the temperature and blue marks represent decreasing.

The effect of annealing can also be characterized quantitatively by the ratio of resistances at selected temperatures. For example, for sample C247#9 from Figures 6.8 and 6.9 can be obtained $R_{280}/R_{25} = 2.04$ in the as-grown state (not previously heated) and $R_{280}/R_{25} = 2.56$ after annealing. The ratio of resistance after annealing and in the as-grown state is $R_{ann/ag} = 1.95$ at 25 °C. Values of the resistance ratios for all samples will be summarized in Table 6.2 later in the chapter.

Another set of measurements was done to investigate the hysteresis in the temperature measurement more deeply. This measurement demonstrated that the width of the hysteresis loop depends on the ramping speed with which the temperature changes. In Figure 6.10, the outer loop (the rightmost red curve and the leftmost blue curve) corresponds to ramping speed of approx. 20 °C/min while the inner loop corresponds to approx. 2 °C/min. Each of the measurements presented in this work (except this one) was done at the ramping speed of approx. 20 °C/min.

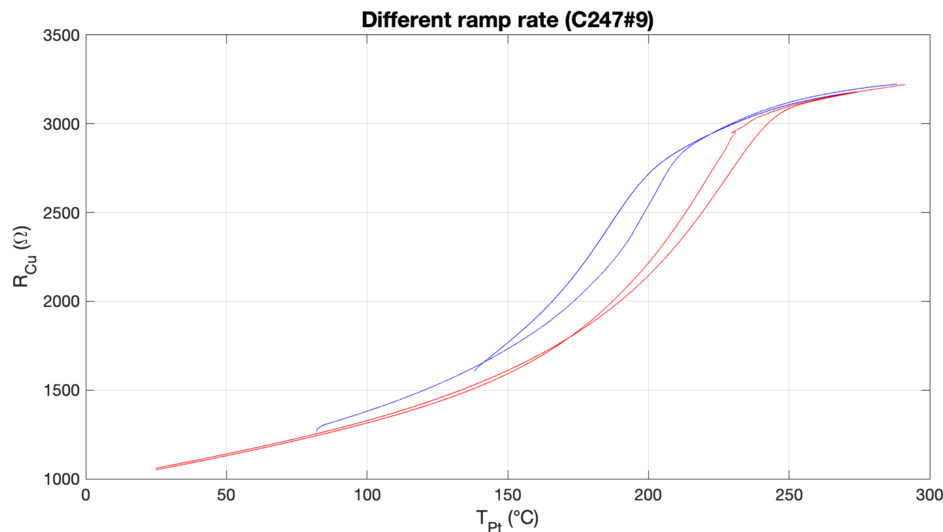

Figure 6.10: Temperature dependencies of CuMnAs sample measured with two different ramping speeds.

6.3.3 Verification by SEM images

The lithographically prepared CuMnAs chip was examined using a scanning electron microscope located in the clean room laboratory and measured right after fabrication and then again after several measurements in high temperatures and its corresponding annealing. This investigation aimed to ensure the integrity of the lithographic process and to assess any potential damage to the CuMnAs structure and the accompanying platinum thermometer that could have happened during the measurement.

Observing Figure 6.11, no distinct changes can be seen in the SEM images of the bar channels of the CuMnAs, and no notable decrease in the thickness of the 3 μm thin platinum channel happened. These findings strongly indicate the robustness of the lithographic process, and they provide reassurance that the conducted measurements did not harm the integrity of the sample.

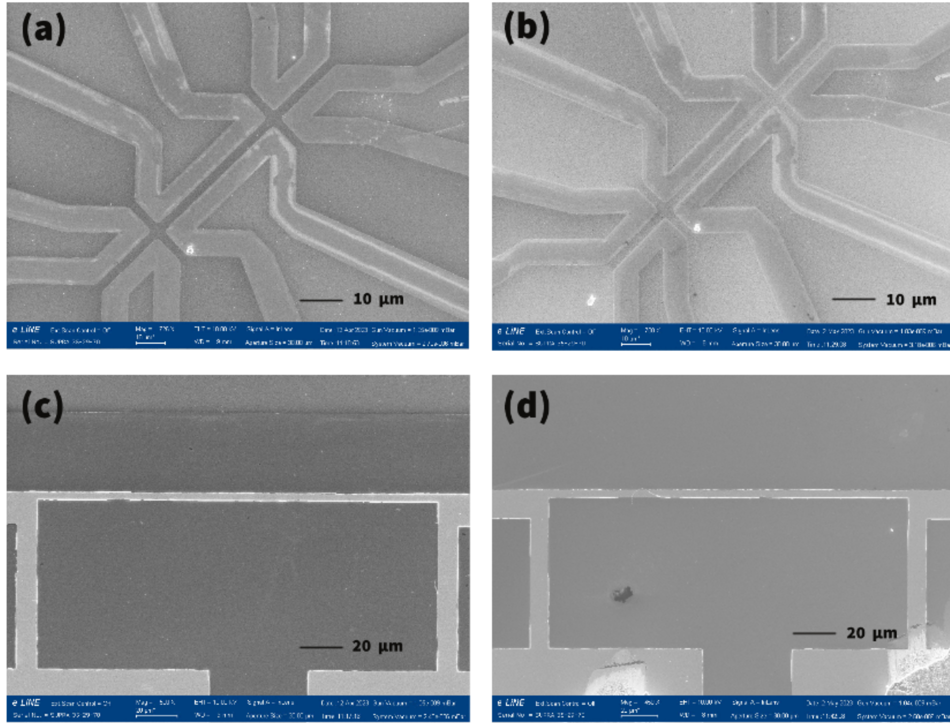

Figure 6.11: SEM images of D210#2 sample: (a) bar structure before measurement, (b) bar structure after measurement, (c) platinum channel before measurement, (d) platinum channel after measurement.

6.4. Discussion

The first point of the discussion returns to the complex approach of the data procession from the thin-layer platinum thermometer. The Pt100 sensors are known to be good heater elements, having a linear dependence of resistance on a temperature which can be easily computed into temperature. However, as described in [26], Pt100 has these good properties only as a bulk material, and its thin layer is unfortunately prone to annealing. To account for this, the final resistance-temperature calibration incorporates results from the bulk Pt100 sensor, the thin-layer platinum, and the tungsten wire resistance measured during the same heating process. Consequently, the fitted temperature function can be deemed sufficiently precise for these high-temperature measurements.

Reviewing the measurement results of GaP-grown CuMnAs, on the as-grown camples there is typically no sign of the magnetic phase transition on the R(T) or dR/dT lines up to 270 °C. This can be explained by the fact that the epitaxial film, always somewhat strained by the mismatch between the substrate and the film, may exhibit a higher critical temperature than the bulk material. Only after a certain degree of annealing does a distinct maximum on the dR/dT appear that likely indicates the Néel temperature. This resembles the behavior of the Curie-point singularity observed in (Ga,Mn)As [27], where also the critical temperature corresponds to the maximum of the derivative function.

The same method was applied to the CuMnAs measurements; however, two different maximums were observed on the derivative curves, one during heating and another one during cooling. This observation may be linked to the slow dynamics associated with the

creeping of structural defects. Lowering the critical point altogether may correspond to the heat-assisted relaxation of the strain induced by the lattice mismatch. With extended annealing (in this case, 2 hours at 280 °C), the critical temperature saturates at approximately 225 °C (498 K), slightly higher than the previously reported value of (480 ± 5) K.

Another strong indication pointing to an involvement of magnetic order is the observed hysteresis, particularly the collapsing of the heating and cooling curves into one at higher temperatures. On the other hand, considering its slow dynamics, magnetism is unlikely the only origin of the effect. It is more probable that some mechanism involving structural defects, induced or promoted by factors such as the magnetoelastic effect, is at play.

The idea of the involved slow dynamics of moving structural defects seems to be supported by the narrowing of the hysteresis with decreasing ramping speed shown in Figure 6.10. One can assume that it disappears completely at an extremely slow ramp. Unfortunately, such an experiment would have to last at least several days, making it challenging to conduct.

The height of the dR/dT maxima, or the 'sharpness' of the magnetic phase transition, increases to some degree with the annealing. However, it can be expected (although it was not explored in this work) that an excessively high annealing temperature would lead to structural instability and an irreversible change in the material structure. No structural or morphological changes were, however, found in our case, as confirmed by the SEM images.

6.5. Comparison of different CuMnAs samples

After the temperature measurement process and the typical temperature dependencies of CuMnAs thin film were shown and discussed, now is presented a comparison of measured samples, focused on their crystallographic orientation, thickness, and types of substrates. A discussions follows the comparison results in each section.

6.5.1 Comparison of different 20 nm GaP CuMnAs samples

Temperature dependences of 20 nm thin samples grown under slightly different growth conditions are shown in Figure 6.12. In general, their behavior is similar to the typical one described in the previous section. However, two new features can be observed.

First, one of the samples, D205#3, does not display the hysteresis in resistance. To verify this finding, two samples with different crystallographic orientations were made of the same layer, and the absence of hysteresis was confirmed, see the right panels of Figure 6.12. Similarly, the presence of hysteresis was confirmed in a second sample (with a different orientation) of layer C247#10 (not shown in the Figure 6.12). This verifies that individual samples fabricated from one layer always behave consistently, which indicates that the bistability is a property of the material rather than that of the individual sample. The origin of the absence of hysteresis remains unclear. It can possibly be attributed to a large density of structural defects in the sample, whose effect on the dynamics averages out. This explanation seems to be supported by the comparably higher resistance of layer D205#3.

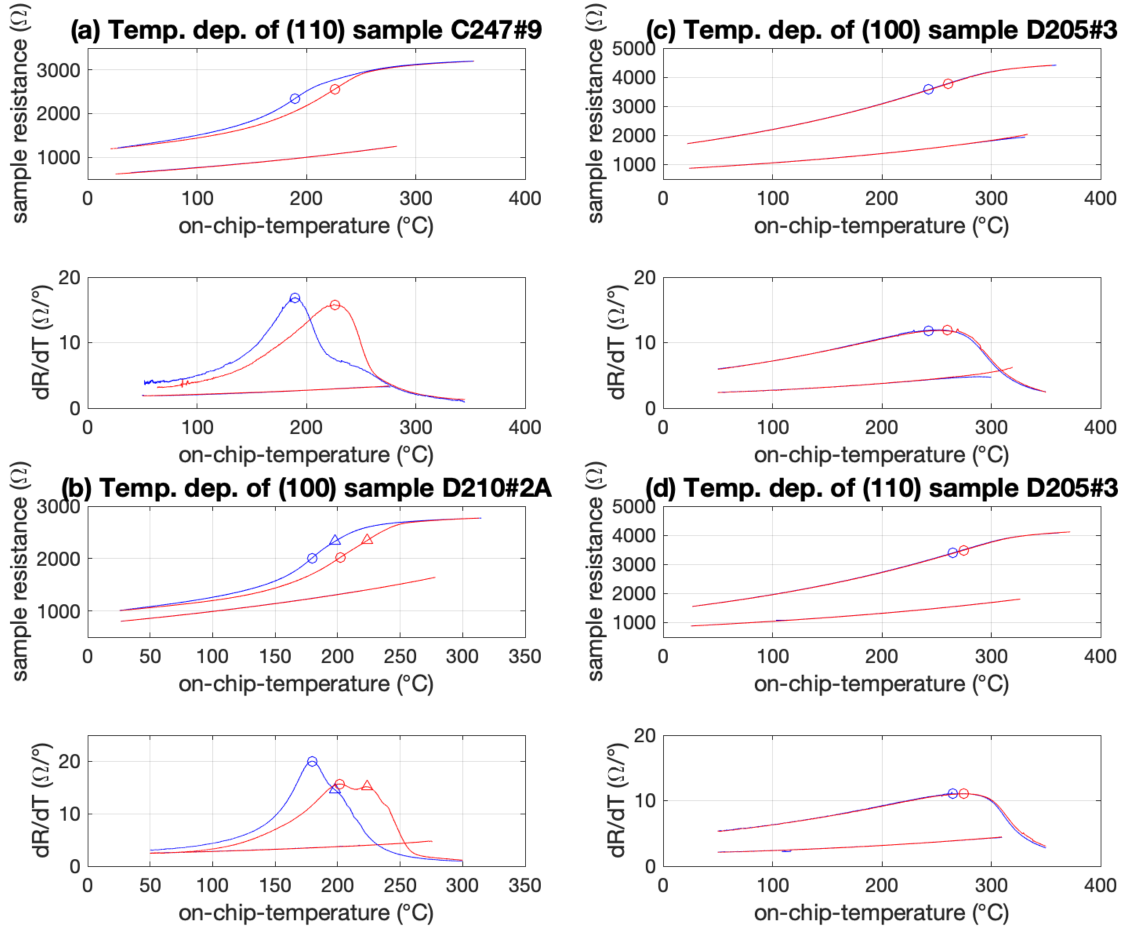

Figure 6.12: Comparison of temperature dependencies of three different 20 nm CuMnAs samples on GaP substrates.

Second, a second, less distinct maximum appears on the dR/dT curve of one sample and an indication of such a second emerging maximum can be traced in another one. We may attribute this to the formation of crystallite grain(s) with different critical temperatures or to a particular configuration of structural defects.

6.5.2 Comparison of thicknesses of GaP CuMnAs samples

The next comparison focuses on GaP samples with different thicknesses. While the as-grown conductance monotonously increases with increasing thickness, the thickness dependence is not linear with the conductance parameter, with the 20 nm sample having the largest conductance per unit of thickness. The critical temperature increases with thickness as well.

In Figure 6.13 (a), the 10 nm sample demonstrates slower dynamics compared to the 20 nm sample in Figure 6.13 (b), leading to a hysteresis loop that is open at all measured temperatures. Contrary to that, the 50 nm sample does not exhibit bistability. Building on the logic from the previous comparison, a thick sample contains more structural

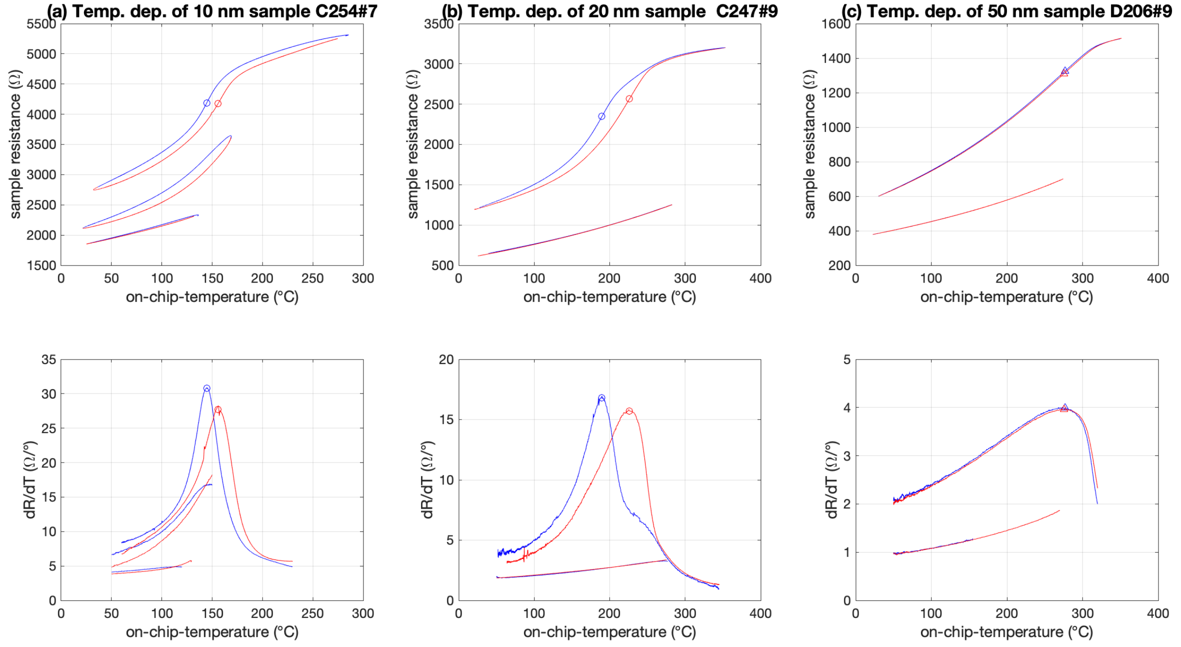

Figure 6.13: Comparison of temperature dependencies of CuMnAs samples with various thicknesses grown on GaP substrates.

defects, which may statistically average themselves, resulting in the absence of pronounced bistability. This reasoning is again further supported by the initial resistance, which is much higher than expected.

6.5.3 Comparison of different substrates

The last comparison attempted to measure and analyze 20 nm CuMnAs samples on different substrates. While the samples on the GaP substrate allowed for the CuMnAs layer to be measured, the same can not be said about the GaAs and Si substrates. Both substrates showed strange local maximums during the measurements, immediately recognized as not belonging to the CuMnAs properties.

To prove that the measured parameters are affected by the different substrates, the measured resistance was converted to conductance S_{CuMnAs}, as seen in Figure 6.14. Linear fit S_{lin} was then calculated for values below 100 °C and extrapolated to high temperatures. The substrate conductance was assumed as $S_{sub}(T) = k \cdot n(T) = T^{3/2}\ exp[-E_G/(k_B T/e)]$, using the standard formula for the carrier density in a semiconductor. Constant k was then adjusted to match the total sample conductance S_{CuMnAs} by the sum of $S_{sub} + S_{lin}$.

This computation was done for both the GaAs and Si substrate, and both resulting functions matched the measured conductance very well. It is then safe to say that the observed maximums were due to the parallel conductance of the substrates rather than a feature of CuMnAs, and further measurements would not bring any fruitful information.

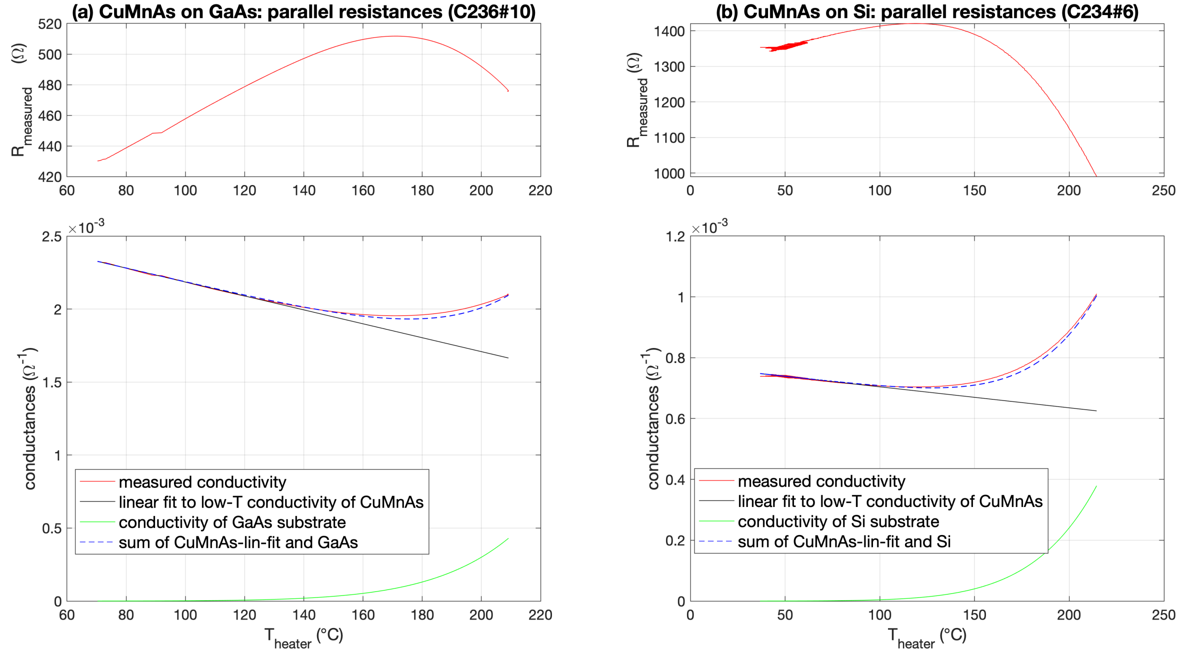

Figure 6.14: Comparison of measured resistances of 20 nm CuMnAs samples grown on (a) GaAs substrate and (b) Si substrates.

6.5.4 Final results

Finally, all the results of temperature measurements are quantitatively summarized in Table 6.2.

sample	subs.	t [nm]	R_{ag}	R_{an}/R_{ag}	R_{280}/R_{25}		T_{N}	T_{N}
			at 25°C		as gr.	ann.	up	down
C234#6	Si	20	1470					
C236#10	GaAs	20	1002.2					
C247#9	GaP	20	615.7	1.95	2.04	2.56	226	190
C254#7	GaP	10	1851.5	1.46		1.96	156	145
D205#1	GaP	20	872.6	1.99	1.97	2.31	275	265
D206#9	GaP	50	380.4	1.56	1.87	2.26	276	277
D210#2	GaP	20	800	1.25	2.08	2.73	202	179

Table 6.2: A summary of all the measured samples, their basic properties, and their measured temperatures, temperature ratios either in the as-grown or annealed state and the determined Néel temperatures measured while ramping up or down. All the temperatures are in °C and resistances in Ω.

7. Chapter
Conclusion

In conclusion, this thesis has provided an overview of the principles and materials used in spintronics devices and explained the potential of replacing traditional ferromagnets with new antiferromagnetic compounds. The thesis mainly focused on CuMnAs as a potential material for spintronic applications, giving a more detailed description of its unique properties. The experimental part of the study involved the design and realization of a new set-up to measure the temperature dependence of the resistivity of thin film CuMnAs samples prepared by MBE. The key point of the design was a dedicated Pt sensor lithographically fabricated along the CuMnAs sample on the same chip. The inevitable annealing effect initially occurring in the thin-film Pt was eliminated by a proper calibration procedure, and the high-vacuum environment suppressed sample degradation.

While confirming some known or expected facts, the experimental findings have revealed several new important insights. Firstly, it was observed that the resistance of CuMnAs undergoes a significant and irreversible change when heated above 250°C, which, however, can not be attributed to simple degradation or surface oxidation. Scanning electron microscopy also observed no changes in the surface morphology. Change in the resistance at a given temperature saturates in time, indicating the presence of an annealing effect. This change in resistance is accompanied by a transition in the R(T) dependence from a flat featureless function to a double-bent function with a clear inflection point, indicative of the Néel temperature.

Furthermore, the annealing process leads to the formation of a hysteretic loop in the temperature dependence of the resistance, suggesting the presence of slow relaxation processes associated probably with structural defects. On the other hand, as the hysteresis disappears above the Néel temperature, some interplay between the structural defects and the magnetic ordering must be assumed. Surprisingly, some samples do not exhibit the hysteresis in the resistance and it was proven that this is a property of the epitaxial CuMnAs layer rather than that of the individual sample. A clear correlation with other parameters of the particular sample or the particular material is, however, yet to be identified.

Systematic studies on a series of different samples revealed that the critical temperature increases with increasing thickness, and samples with a moderate thickness (ca. 20 nm) grown on GaP exhibit the best specific conductivity.

These findings pave the way for further research directions, including a quantitative investigation of the slow dynamics, microscopic examination of the correlation between resistance and structural changes, and experiments involving fast (e.g. optical) heating techniques to suppress the annealing effect.

Overall, this thesis contributes to the understanding of CuMnAs as a potential material for spintronic applications and highlights the importance of further exploring its properties and behavior in order to advance the field of spintronics.

Bibliography

[1] Schäpers, Thomas, *Semiconductor Spintronics*. Berlin, Boston: De Gruyter, 2021.

[2] Claudia Felser, Gerhard H. Fecher, *Spintronics: From Materials to Devices*. Springer, 2013.

[3] S. A. Wolf, et al, *Spintronics: A Spin-Based Electronics Vision for the Future*. Science 294, 1488-1495, 2001.

[4] Dieny, B., Prejbeanu, I.L., Garello, K. et al, *Opportunities and challenges for spintronics in the microelectronics industry*. Nat Electron 3, 446–459, 2020.

[5] Samal, Dibyajyoti, Kumar, Anil, *Giant magnetoresistance*. Resonance. 13. 343-354, 2008.

[6] Liu Chang, Min Wang, et al, *A brief introduction to giant magnetoresistance*. Ltd., Beijing, China, Ohio State University, Columbus, OH 43210.

[7] Wikipedia, the free encyclopedia, *Tunnel magnetoresistance*. https://en.wikipedia.org/wiki/Tunnel_magnetoresistance

[8] Sabpreet Bhatti, Rachid Sbiaa, Atsufumi Hirohata, Hideo Ohno, Shunsuke Fukami, S.N. Piramanayagam, *Spintronics based random access memory: a review*. Materials Today, Volume 20, Issue 9, 2017, Pages 530-548, ISSN 1369-7021.

[9] Rajesh Saha, Yogendra Pratap Pundir, Pankaj Kumar Pal, *Comparative analysis of STT and SOT based MRAMs for last level caches*. Journal of Magnetism and Magnetic Materials, Volume 551, 2022, 169161, ISSN 0304-8853.

[10] Minh-Hai Nguyen and Chi-Feng Pai, *Spin–orbit torque characterization in a nutshell*. APL Materials 9, 030902, 2021.

[11] Gomonay, O.; Jungwirth, T.; Sinova, J., *Concepts of antiferromagnetic spintronics*. Physica Status Solidi RRL. Wiley. 11 (4): 1700022, 2017.

[12] Sugahara, S., & Nitta, J., *Spin-Transistor Electronics: An Overview and Outlook*. Proceedings of the IEEE, 98, 2124-2154, 2010.

[13] Datta, S., *How we proposed the spin transistor*. Nat Electron 1, 604, 2018.

[14] Sarkar, Kingshuk & Aharony, Amnon & Entin-Wohlman, O. & Jonson, M. & Shekhter, Robert, *Datta-Das spin field-effect transistor under various magnetic fields*. 2020.

[15] Koo, H. C., Kwon, J. H., Eom, J., Chang, J., Han, S. H., & Johnson, M., *Control of Spin Precession in a Spin-Injected Field Effect Transistor*. Science, 325(5947), 1515–1518., 2009.

[16] Katherine L. Wellmon, *Antiferromagnetism*. LibreTexts Engineering. https://eng.libretexts.org/Bookshelves/Materials_Science/Supplemental_Modules_(Materials_Science)/Magnetic_Properties/Antiferromagnetism

[17] Zheng-Fei Guo et al, *Electrochromic & magnetic properties of electrode materials for lithium ion batteries*. Chinese Phys. B 25 0178014, 2016.

[18] Sanghoon Lee, J.-H. Chung, Xinyu Liu, Jacek K. Furdyna, Brian J. Kirby, *Ferromagnetic semiconductor GaMnAs*. Materials Today, Volume 12, Issue 4, 14-21, 2009.

[19] Aravind, A., Jayaraj, M.K., *Zno-Based Dilute Magnetic Semiconductors*. Nanostructured Metal Oxides and Devices. Materials Horizons: From Nature to Nanomaterials. Springer, Singapore, 2020.

[20] Yakout, Saad Mabrouk, *Spintronics: Future Technology for New Data Storage and Communication Devices*. Journal of Superconductivity and Novel Magnetism. 33. 10.1007/s10948-020-05545-8, 2020.

[21] Wadley, P., Novák, V., Campion, R. et al, *Tetragonal phase of epitaxial room-temperature antiferromagnet CuMnAs*. Nat Commun 4, 2322, 2013.

[22] Nils Sommer, *Critical domain wall behavior in chiral magnetic nanowires induced by spin polarized currents*. Master Thesis in Physics submitted to the Department of Physics, Mathematics and Computer Science of Johannes Gutenberg-Universität Mainz, 2019.

[23] P. Wadley, et al, *Electrical switching of an antiferromagnet*. Science 351, 587-590, 2016.

[24] Kašpar, Z., Surýnek, M., Zubáč, J. et al, *Quenching of an antiferromagnet into high resistivity states using electrical or ultrashort optical pulses*. Nat Electron 4, 30–37, 2021.

[25] Wadley, P., Hills, V., Shahedkhah, M. et al, *Antiferromagnetic structure in tetragonal CuMnAs thin films*. Sci Rep 5, 17079, 2015.

[26] U. Schmid, H. Seidel, *Influence of thermal annealing on the resistivity of titanium/-platinum thin films*. Journal of Vacuum Science & Technology A 24, 2139–2146, 2006.

[27] V. Novák, K. Olejník, J. Wunderlich, et al, *Curie Point Singularity in the Temperature Derivative of Resistivity in (Ga,Mn)As*. Phys. Rev. Lett. 101, 077201, 2008.

[28] Filip Krizek, Zdeněk Kašpar, Aliaksei Vetushka, Dominik Kriegner, et al, *Molecular beam epitaxy of CuMnAs*. Phys. Rev. Materials 4, 014409, 2020.

[29] W. P. Mccray, *MBE deserves a place in the history books*. Nature nanotechnology, 2 5, 259-61, 2017

[30] *Global Molecular Beam Epitaxy (MBE) Market Expected to Witness a Sustainable Growth over 2025*. https://www.openpr.com/news/2138968/global-molecular-beam-epitaxy-mbe-market-expected-to-witness